www.sciencemag.org/cgi/content/full/science.1241514/DC1

Supplementary Material for

Waveform Tomography Reveals Channeled Flow at the Base of the Oceanic Asthenosphere

Scott French, Vedran Lekic, Barbara Romanowicz*

*Corresponding author. E-mail: barbara@seismo.berkeley.edu

Published 5 September 2013 on *Science* Express
DOI: 10.1126/science.1241514

This PDF file includes:

Supplementary Text

Motivation

These materials are intended to provide support to inferences appearing in the main text. In particular, we describe the provenance of the updated SEMum (*11*) model, upon which our analysis is based (Section S1). We also present a systematic series of tests that quantify model performance (Section S2) as well as resolution and uncertainties (Section S4). We analyze the effects of three different sources of error on our model: 1. Uncertainty in the surface-wave dispersion measurements used to constrain crustal structure; 2. Potential bias due to parameterization of crustal structure; and 3. Uncertainty due to noise in the waveform dataset. Further, we carry out four different types of error analysis to quantify the reliability of our tomographic model: 1. Standard linear resolution analysis using a resolution operator; 2. Bootstrap analysis of stability of model structure; 3. Independent validation against waveform data that (a) were not used in the construction of the tomographic model and (b) extend to shorter periods than used in the inversion; and 4. Independent validation against structures inferred by regional / smaller-scale studies. Additionally, we present further discussion of: (a) the oceanic upper-mantle cluster analysis of SEMum2 (Section S3), (b) the model of absolute plate-motion cited in the main text (Section S5.1), and (c) thermal implications of imaged V_S structures (Section S5.2).

S1 The SEMum and SEMum2 models

The SEMum model (*11*) was the first global upper-mantle shear-velocity model developed using full waveform inversion combined with spectral-element forward modeling (SEM: e.g. (*31*)). This model was constructed using both fundamental-mode and overtone waveforms observed on both minor and major arcs ((X)R1/G1 and (X)R2/G2) and filtered at periods longer than 60s, which were inverted by iteratively minimizing the L_2 misfit function defined over differences between time-discretized waveform data $\mathbf{d}$ and SEM synthetics $\mathbf{g}(\cdot)$ given the current model estimate $\mathbf{m}$: $[\mathbf{d} - \mathbf{g}(\mathbf{m})]^T \mathbf{C}_d^{-1} [\mathbf{d} - \mathbf{g}(\mathbf{m})]$ (where $\mathbf{C}_d$ reflects data uncertainties and uniqueness – see (*11*)). Importantly, this choice of misfit function retains both phase *and* amplitude information. These data were collected from a combination of 203 shallow and deep earthquakes well-distributed globally in the years 1993-2007 – amounting to nearly 99,000 waveform windows and containing over 5 million data points. Partly because SEM-based forward modeling fully accounts for phenomena such as focusing and wavefront healing, SEMum is characterized by stronger lateral heterogeneity in the upper 250 km – particularly in low velocities – than previous global models derived with approximate forward-modeling techniques (*13*). In our present work, we discuss the structure of an updated SEMum model (hereafter: SEMum2) derived using the same methods, but with two key improvements aimed at enhanced recovery of oceanic upper-mantle structure: 1. A new implementation of the crustal modeling scheme; and 2. Inversion for shorter-wavelength mantle structure, supported by a change in parameterization and resolution tests.

S1.1 Crustal modeling

To render SEM computations tractable, SEMum used long-period waveform data (60-400s) combined with a 60 km-thick crustal layer, whose seismic response is equivalent to that of the Earth's true crust in the frequency range of interest. This smooth *equivalent* crust enabled us to avoid computationally costly (*31*) meshing of a thinly-layered crustal model, which would necessitate a very small time step to ensure accurate wave propagation calculations. In order to match the seismic response of a thinly-layered crust, spatially-varying radial anisotropy was introduced (*32,33*). Though the velocity profiles of the 60 km equivalent crust may be similar to the true velocity profiles in continental settings, albeit smooth, the imposition of the thick equivalent crustal layer may complicate interpretation of shallow upper-mantle structure in oceanic regions (above 80 km). To remedy this, we modified the crustal layer, so that now its thickness approximately honors that of Crust2.0 (*34*) in continental regions, while it is fixed at 30 km in the oceans. Anisotropic velocity structure of the crustal layer is parameterized in the same Lagrange polynomials as used in the SEM, similar to the crustal-modeling approach shown to be effective by Fichtner & Igel (*35*). Like the original crustal model, the new equivalent crustal layer is calibrated to match global 25-60s group-velocity dispersion maps (*36,37*). Calibration proceeds in two inverse modeling steps: 1. An initial grid search for best-fitting isotropic crustal models; and 2. An iterative inversion introducing radial anisotropy, necessary to fit both Rayleigh and Love wave dispersion (*32*). Convergence in step 2 is defined to be achieved when the mean misfit between group velocities predicted from the crustal model and those from the 25-60s dispersion maps falls below 50m/s.

Uncertainty due to group-velocity dispersion data

We find it preferable to match these dispersion data directly, reflecting the integrated effect of Earth's crust on the wavefield, rather than matching dispersion predicted by an a priori model with poorly quantified uncertainties. Still, the dispersion maps also have associated uncertainties (*37*), so it is reasonable to ask whether error in the maps, absorbed into the crustal layer, can significantly affect the long-period wavefield and in turn bias our mantle model. To answer this question, we built an ensemble of crustal models following the 2-step procedure above, again derived from 25-60s dispersion maps, but now with added Gaussian noise (σ=40m/s, similar to uncertainties reported in (*37*)). We calculated SEM synthetics in the period band of our mantle inversion (60-400s) for each crustal-layer realization and examined variation in the resulting waveforms. As seen in Figure S1 for a representative event from our dataset, the ensembles of synthetic traces clearly do not differ significantly. Thus, we are confident that variation in crustal-layer velocity structure due to uncertainties in the dispersion maps cannot appreciably bias our mantle model.

Uncertainty due to crustal parameterization

A second potential source of model uncertainty is systematic error due to parameterization. In particular, we ask whether our choice of Lagrange interpolants or scaling relations for ρ and V_P (*38*) can adversely affect the 60-400s waveforms in our mantle inversion – especially in the case of oceans, where the 30 km crustal-layer

thickness should necessitate larger velocity and radial-anisotropy variations than required in continents, in order to match the observed dispersion. To answer this question quantitatively, we calculated synthetic 25-60s dispersion data for an ensemble of realistic thinly layered oceanic crustal structures (Crust2.0 (*34*) with randomly-perturbed layer thicknesses) atop oceanic upper-mantle structure sampled from SEMum2. We fit the synthetic data using the 2-step scheme above, and compared full long-period waveforms (60-400s) calculated for the input layered models and the output models with a 30 km crust. Illustrated in Figure S2, the results confirm that parameterization – which is the only source of errors in these noise-free tests – has a negligible effect on long-period waveforms: both fundamental-mode and overtone wavetrains generally show excellent fits between the layered and 30 km smooth-crust models.

S1.2 SEMum2 mantle-model update

The SEMum2 model reflects two additional iterations of the SEM-based "hybrid" waveform inversion scheme employed by (*11*) following the introduction of the new crustal layer, as well as one further iteration following a change in parameterization of the mantle model. The hybrid scheme was motivated by the fact that, under the generalized-least squares formalism for non-linear inverse problems (*39*), error in solving the forward problem (waveform-modeling) appears as a first-order term in the expression for the retrieved model, while error in partial derivatives (sensitivity kernels) has a second order effect [e.g. Appendix A of (*11*)]. In other words, it is more important to be solving the correct problem – and thus seek the correct minimum – than to estimate the optimal descent direction. To this end, the hybrid approach uses the SEM to solve the forward problem "exactly" along with approximate sensitivity kernels from non-linear asymptotic coupling theory (NACT: (*40*)). For a detailed description of this technique, we refer the reader to (*11*). Although they do not include effects outside of the vertical plane containing source and receiver, as would sensitivity kernels calculated with a SEM-based adjoint method (*41*), the NACT kernels offer several advantages: 1. In addition to being updated at each iteration, the kernels include multiple forward scattering; 2. The kernel computation, based on asymptotic mode coupling, is much faster than a SEM-based adjoint computation; and 3. NACT provides direct access to waveform partial derivatives, allowing the use of a Gauss-Newton inversion scheme, which is known to converge faster than the conjugate gradient scheme necessary in adjoint-type inversions.

Both the SEMum and SEMum2 mantle models are parameterized laterally in spherical splines (*42*) and radially in cubic b-splines (*43*). Similarity between the long-wavelength structure of SEMum and that obtained with the refined crustal model and additional iterations of SEMum2 strongly suggested that the iteratively linearized tomographic inversion had converged. This fact, combined with the excellent recovery of small-scale structures apparent in the resolution operator analysis of SEMum (see (*11*)), motivated us to refine the lateral parameterization of SEMum2, which would allow us to recover more detailed images of the deep low-velocity structures discussed in the main text. We did so by halving the spherical-spline knot spacing used for isotropic V_S in SEMum2, from 4° to 2° and performing an additional waveform-inversion iteration, reducing the minimum a priori correlation length for V_S permitted in our formulation (*39*) from 800 km to 400 km (see (*11*) for details). While we could not rule out ahead of time

the possibility that no additional recoverable information was present in the waveform data and that we would fit noise, we subsequently verified that this was not the case in two ways. First, we performed an additional resolution analysis, which demonstrated that structures smaller than those permitted by the previous lateral parameterization could indeed be retrieved (this statement should be interpreted with the usual caveats regarding checkerboard tests, see Section S4.1). Second, the inversion with the finer parameterization resulted in improved fits for data that were not originally included in the inversion; among this held-out data, 168 additional waveform windows (fundamental and/or overtone-mode wavetrains), previously excluded from the inversion due to large residuals, became admissible. Thus, together with the demonstrations of model performance in Section S2, we are confident that our progression to shorter-scale structure is justified.

S2 Model performance and validation

S2.1 Data and variance reduction

In Table S1, we summarize SEMum2 performance in terms of waveform variance reduction, listed for each component and windowed-wavetrain type separately, in addition to the corresponding numbers of windows and data points contained therein. In total, our dataset contains more than 99,000 individual windowed wavetrains, corresponding to over 5,200,000 data points (sampled at 30s – the Nyquist limit for our 60s minimum-period – implying maximal independence between neighboring points without information loss). We note that our fundamental-mode and overtone waveform dataset is considerably *larger* than that used in previous global models from our group (see Table 1 of (*44*), for comparison). Further, considering total number of data points alone, 5.2M surpasses previous UCB whole-mantle models even when including their extensive body-waveform datasets (*44*).

S2.2 Independent validation

Waveform fits for earthquakes not in our dataset, and at periods shorter than used in our inversion, provide another way to evaluate model performance. We demonstrate this ability to *generalize* in Figure S3, where we observe close fits between data and synthetics, particularly in phase but also in amplitude, now calculated down to 40s instead of the 60s cut-off for waveforms used in the inversion, and for 3 events not previously included in our modeling. Performance may also be quantified in terms of surface-wave dispersion. In Figure S4 we compare phase velocities measured from both the observed data and SEMum2 synthetics, again for an event not included in our inversion, using the multitaper technique of (*45*). We find that dispersion fits are quite good – in general within 10m/s where the measurements remain stable – and further represent a conservative estimate of model quality, given the sensitivity of single-station phase measurements to source uncertainty (at least for observed data – sources used in the SEM are well defined). Further, Figure S4 also includes phase velocities inferred from the single-station phase-anomaly dataset of (*46*) (where available), which are in general compatible with our measurements to within associated uncertainties.

S2.3 Comparison to other models

Global V_S structure in the SEMum2 model is shown in Figure S5 at a number of upper-mantle and transition-zone depths, accompanied by structure from the recent global models of Kustowski et al. (*47*) and Ritsema et al. (*48*). While the three models agree well at long wavelengths, it is clear that SEMum2 is characterized by stronger, more-focused anomalies. Local- and regional-scale tomography provides an additional avenue for model validation: especially important given the unusually large-amplitude heterogeneity in SEMum2 (e.g. low-velocity anomalies beneath the East Pacific Rise consistently in excess of 9%). In Figure S6, we show 1D V_S profiles from SEMum2 and the same two recent global models (*47,48*), collocated at the EPR with the OBS-based tomographic study of (*49*) for which we show a 1D-mean centered on the ridge axis (averaging over approximately one SEMum2 correlation length; Section S1.2). While structure above 50 km cannot be interpreted due to the 30 km crustal layer (Section S1.1), SEMum2 recovers both the strength and depth of the low-velocity zone beneath the EPR imaged by (*49*) far more closely than either of the other global models. With this local validation of amplitudes in mind, we compare SEMum2 Pacific upper-mantle and transition-zone cross-sections to these same two global models in Figures S7 and S8. We see that SEMum2 amplitudes are systematically stronger, particularly for low velocities, while morphology of structure is generally consistent at long wavelengths. Notably, SEMum2 structure appears more concentrated and contiguous, particularly in the images of subducted slabs and columnar low-velocity features discussed in the main text (e.g. beneath the Pacific Superswell (*12*)).

S3 Cluster analysis

Given an ensemble of data points distributed among a set of *clusters* – defined by their means, which are not known a priori – as well as an assumed *number* of clusters, the k-means algorithm (*50*) provides an objective estimate of both the unknown means and data-point partitioning. As shown in (*13*), this technique can be applied to V_S profiles sampled from tomographic models to discover objective *classes* of model structure – both their lateral extent and appearance. We applied this analysis to oceanic upper-mantle (30-350 km) structure in SEMum2, and feature a pertinent subset of the results in Figure 1 of the main text. For completeness, the full results can be found in Figure S9, showing global distribution of the structural classification, as well as more-detailed characterization of intra-cluster variation. Further, to estimate uncertainties in the cluster centroids, we repeat the cluster analysis for each of the bootstrap models obtained in Section S4.2 below, and show the resulting ensembles of cluster-centroid profiles in panel (B) (analogous to the SEMum2 cluster centroids shown in panel (B) of Figure 1). We note that the 2σ uncertainty characterizing each ensemble of profiles is indistinguishable from the width of the ensemble itself at this plotting scale. Indeed, it is clear that the different classes of SEMum2 structure revealed by the cluster analysis remain distinct at the 2σ level, much like the underlying V_S anomalies associated with the LVFs, as discussed below in Section S4.2 and demonstrated in Figure S14.

S4 Resolution and uncertainties

S4.1 Resolution analysis

Pitfalls of the "standard" resolution analyses employed in many tomographic studies are well known, including strict validity only for linear problems (*51*) and potential for misleading results (*52*) (see (*15*) for discussion in the context of waveform inversion). Further, such analyses cannot be used to address uncertainties arising from inaccuracy of the modeling theory. Therefore, standard resolution analysis is likely to overestimate the resolution of models constructed using approximate wave propagation approaches compared to those constructed using more accurate wave propagation calculations, such as SEMum and SEMum2. Still, these analyses can provide useful insight on model parameterization and data coverage. Indeed, poor fidelity to a test model (e.g. checkerboard) upon projection onto the model basis clearly implies that structure of similar sharpness or scale cannot be imaged, while data coverage that is too sparse relative to a priori constraints on model smoothness (e.g. correlation length) can result in poor test-model recovery, showing gaps or ray-like smearing – again indicative that small scales may not be well resolved.

Keeping these points in mind, we present resolution analyses for isotropic V_S in Figure S13, using the common checkerboard pattern at global scales, as well as isolated point and band-like structures in the Pacific basin motivated by the columnar anomalies and LVFs. In panel (A), we see that checkerboard inputs are very well retrieved – for both large (2200 km) and small-scale (800 km) structures placed at LVF-relevant depths in equatorial and polar orientations – with no evidence of ray-like smearing or gaps in sensitivity, even at the poles. As such, we expect V_S to be well resolved at 800 km scales in the upper mantle, coincident with the minimum distance of significant correlation permitted in our inversion (2 x 400 km), and only slight degradation in the transition zone – certainly at scales shorter than the well-recovered 2200 km case. In panel (B), we show results for isolated input perturbations at two representative locations to assess vertical smearing: Hawaii, with fairly dense data coverage, and the south-Pacific Superswell (equidistant from Tahiti and Pitcairn) with possibly sparser coverage. Though input amplitudes are not necessarily recovered, morphology with depth is, and we expect accurate distribution of V_S anomalies down to at least 400 km, with only slight vertical smearing below. Finally, in panel (C), we show results for band-like test structures (450 and 900 km widths), concentrated in the 200-350 km depth range, and oriented both normal and parallel to Pacific APM (*14*). Both scales and orientations of bands are well retrieved – demonstrating that: (a) the ~2000 km APM-normal periodicity of the Pacific LVFs cannot be an artifact of our model parameterization or data coverage; and (b) the widths of the Pacific LVFs are well resolved.

S4.2 Uncertainty estimation

While resolution analysis provides a useful assessment of certain aspects of model quality, quantitative estimates of model uncertainties are clearly desirable. One efficient uncertainty-estimation technique is the bootstrap (*53*), in which an ensemble of models is obtained by inverting randomly resampled data and ensemble variation is taken as a

proxy for uncertainty (*44*). Here, for simplicity, we partition our data into 6 subsets (event month modulo 6) and construct resampled data by selecting 4 subsets without and 2 with replacement, such that at most 50% of each resampled set is a *repeated* subset and 33% of available subsets are *missing*. For 20 resampled-data realizations, we re-run the final iteration of our inversion (a Gauss-Newton update scheme forces the model to adjust very quickly to changes in the data). Further, we *do not* reapply our path-weighting scheme (*54*) to the resampled data, increasing the likelihood of large model variations. In Figure S14, we show map views at 250 km depth of both the resulting 2σ uncertainties and SEMum2 V_S structure with regions below the local 2σ masked. Assuming our uncertainty estimates are valid, it is clear that the LVFs are significant at the 2σ level.

S4.3 Stability of model structure

Model structure may further be considered robust if it remains stable following the introduction of new *independent* data. With this in mind, we performed one additional iteration of the hybrid inversion – a hypothetical update to the SEMum2 model – using a new, 144-event waveform dataset that is wholly disjoint from that in our modeling. As noted above (Section S4.2), our use of a Gauss-Newton update scheme implies that model structure should adjust very quickly if required by the new data. In Figure S15, we show V_S structure at 250 km depth in SEMum2 (also shown in Figure 2 of the main text) alongside that from the updated model described here. It is clear that the LVF structures remain stable following application of an independent waveform dataset. Indeed, SEMum2 model structure and that retrieved in the hypothetical update remain correlated at $R>0.95$ when considering up to spherical-harmonic degree 12 and $R>0.9$ to degree 48 throughout the upper mantle. This test again emphasizes the robust nature of the LVF structures seen in the SEMum2 upper mantle.

S4.4 LVF orientations and possible artifacts due to azimuthal sampling

Finally, we wish to explain why the orientations of the LVFs cannot be due to poor azimuthal sampling – either in the form of ray-like smearing or as artifacts of un-modeled azimuthal anisotropy. As noted previously, LVFs tend to align preferentially to APM (*14*), which in turn corresponds to streamlines of solid rotation on the surface of the sphere. Except in the degenerate case arising 90° from the pole of rotation, these paths cannot be fit with a great circle – precluding correspondence between LVFs and ray paths. This point is demonstrated in practice in Figure S16, where we compare LVF orientations from Figure 2(B) in the Pacific and West Antarctic to a sparse, but representative, sampling of rays that traverse these regions from Western-Pacific and Arctic sources to Western-Hemisphere and ocean-island receivers (the distribution of rays when transposing the source and receiver sides would be similar). As expected from the geometric argument above, it is immediately clear from examination of Figure S16 that LVFs cannot be fit by, and cannot correspond to, ray paths. Indeed, this result complements those of our resolution analysis (Section S4.1), which previously ruled-out ray-like smearing. Further, it is extremely unlikely that the LVF structures are artifacts due to un-modeled azimuthal anisotropy, because of two reasons. First, the azimuthal coverage of our dataset is very homogeneous, particularly in the central Pacific, where

the LVFs are most clearly developed (Fig. S17). Second, the bootstrap resampling analysis, which estimates model uncertainties by repeatedly simulating artificially poor data coverage, should yield much larger uncertainties for the LVF structures if our dataset were characterized by uneven azimuthal sampling (Section S4.2, Fig. S14).

S5 Plate motion and temperature models

S5.1 Absolute plate motions

In the main text, we present comparisons between LVF orientations and the absolute plate motion (APM) model of Kreemer (*14*). This APM model combines a comprehensive geodetic dataset, used to constrain relative plate motions, with SKS splitting measurements that constrain the orientation of plate motion relative to the deep mantle – thereby providing an alternative to hotspot-based reference frames, which may be affected by uncertainties in assumed hotspot motion / fixity. Still, this model is consistent with those based on the hotspot frame for the Pacific plate, such as HS3-NUVEL1A (*55*), while showing marked differences in APM direction on several slow moving plates – in particular the Antarctic and African plates (it also reflects different assumptions regarding deformation of the African plate – see (*14*)). Because SEMum2 was constructed using completely independent data and methods from Kreemer's APM model, the striking similarity between plate-motion and LVF orientation in all oceans provides a validation of both models and supports the use of SKS splitting measurements as constraints on the net rotation of the lithosphere with respect to the deep mantle.

S5.2 Temperature variations

Assuming a *purely thermal* origin for lateral V_S variations in the oceanic upper mantle of SEMum2, we estimate corresponding temperature differences to be on the order of 200°C. This estimate is derived using a model of anharmonic V_S temperature dependence for realistic upper-mantle compositions developed by (*56*), and corrected for anelastic dispersion using an ensemble of physically-plausible attenuation models in the manner of (*57*). The latter correction is parameterized in terms of homologous temperature, which in turn relied on upper-mantle solidus temperatures derived by (*58*). Together with absolute V_S from SEMum2, these models form a non-linear system of equations, which may easily be solved numerically – leading to the above estimates of spatial variations in temperature. Importantly, because these estimates assume a purely thermal origin for lateral variations in V_S – ignoring the profound effects of water or partial melt, for example, on shear-wave velocities – they represent *upper bounds* on the associated temperature variations. Future efforts toward SEM-based attenuation tomography will allow for better characterization of the anelastic structure associated with these V_S anomalies, and thus may provide insight on the roles of temperature vs. composition.

S5.3 Comparison with Pacific geoid undulations

As noted in the main text, the ~2000 km wavelength of the LVFs corresponds to a peak in power in Pacific geoid undulations observed by Hayn et al. (*15*), which are also preferentially aligned with absolute plate motion. This geoid signal provides strong evidence for patterns of upper-mantle heterogeneity consistent with the LVFs in both scale and orientation, although it cannot be used to isolate a specific depth range for such features. In Figure S11, we compare the locations and orientations of the LVFs to the distribution of preferential orientation seen in ~1850 km scale Pacific geoid undulations (*15*). Interestingly, the paths associated with the LVFs do not correspond exactly to the broad bands of quasi-APM orientation seen in the geoid: in general, the LVFs fall either between or at the edges of these regions, where more complex variation in preferential orientation of the geoid pattern is observed. In the main text, we note that this observation is not compatible with simple secondary convection in the form of Richter rolls (*1*), where one would expect regular bands of quasi-APM orientation in the geoid to be aligned with the up- (LVF-centered) and down-welling (inter-LVF) limbs. Instead, we note that the observed pattern of preferential geoid orientation may be more compatible with channelization and fingering of plume-fed material in the upper mantle. In this latter case, smaller-scale convective phenomena would be expected to arise within the propagating finger itself (*26*), resulting in more complex local variation in geoid signature. This suggestion could be supported by the imaged variability of shear velocity within the LVFs, which despite being continuous and consistently low-velocity (as demonstrated in the cluster and bootstrap resampling analyses), still exhibit internal V_S minima. Conversely, large expanses of ambient mantle structure between LVF channels are expected to be relatively laterally uniform, and are also APM-aligned – indeed they result from the presence of the through-going LVFs. Therefore, in this scenario, the most laterally coherent regions of APM-parallel preferential orientation in the geoid are actually associated with the comparatively fast bands of ambient mantle, while the system as whole (the ~2000 km periodicity in particular) is controlled by the LVFs.

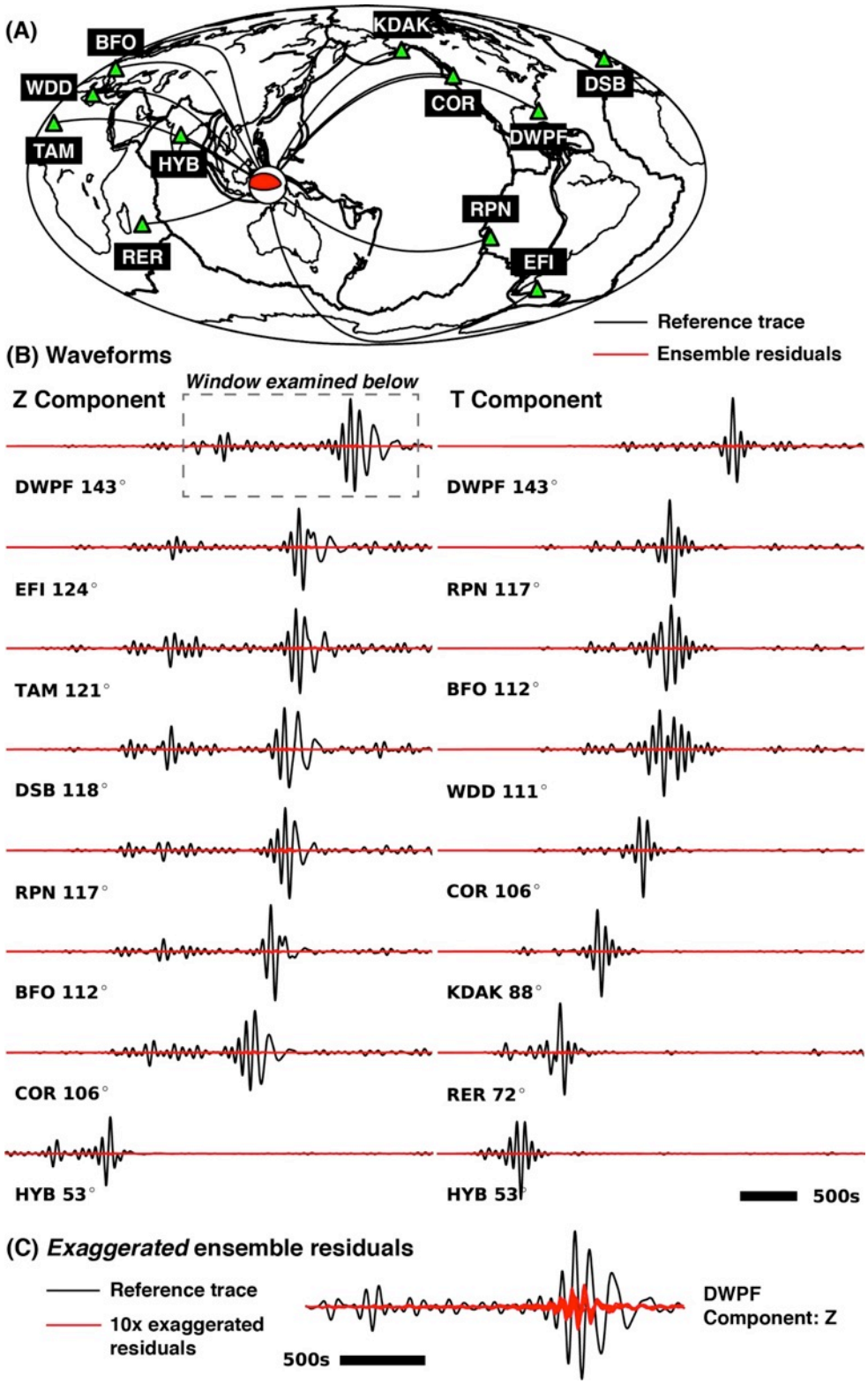

Fig. S1.

Variation in long-period (60-400s) SEM synthetics due to the introduction of realistic-amplitude (*37*) artificial errors into the dispersion maps that form the basis of our crustal-

modeling scheme (Section S1.1). For each path in panel (A) – selected to sample oceanic, continental, and mixed settings – panel (B) shows SEM synthetics calculated in a reference crustal layer (black) for Z (left) and T (right) components, as well as residuals between the reference trace and those calculated in the ensemble of crustal layers based on data with added errors (red). It is immediately apparent that the residuals are very small. Thus, we also show exaggerated (10x) residuals in panel (C), corresponding to the longest path in (B) – traversing both continental and oceanic settings – again illustrating that the apparent variation is not significant. With these results in mind, it is clear that uncertainties in the dispersion data on the order of those reported by (*37*) cannot significantly affect our waveform modeling through contamination of the crustal layer and in turn bias our mantle model.

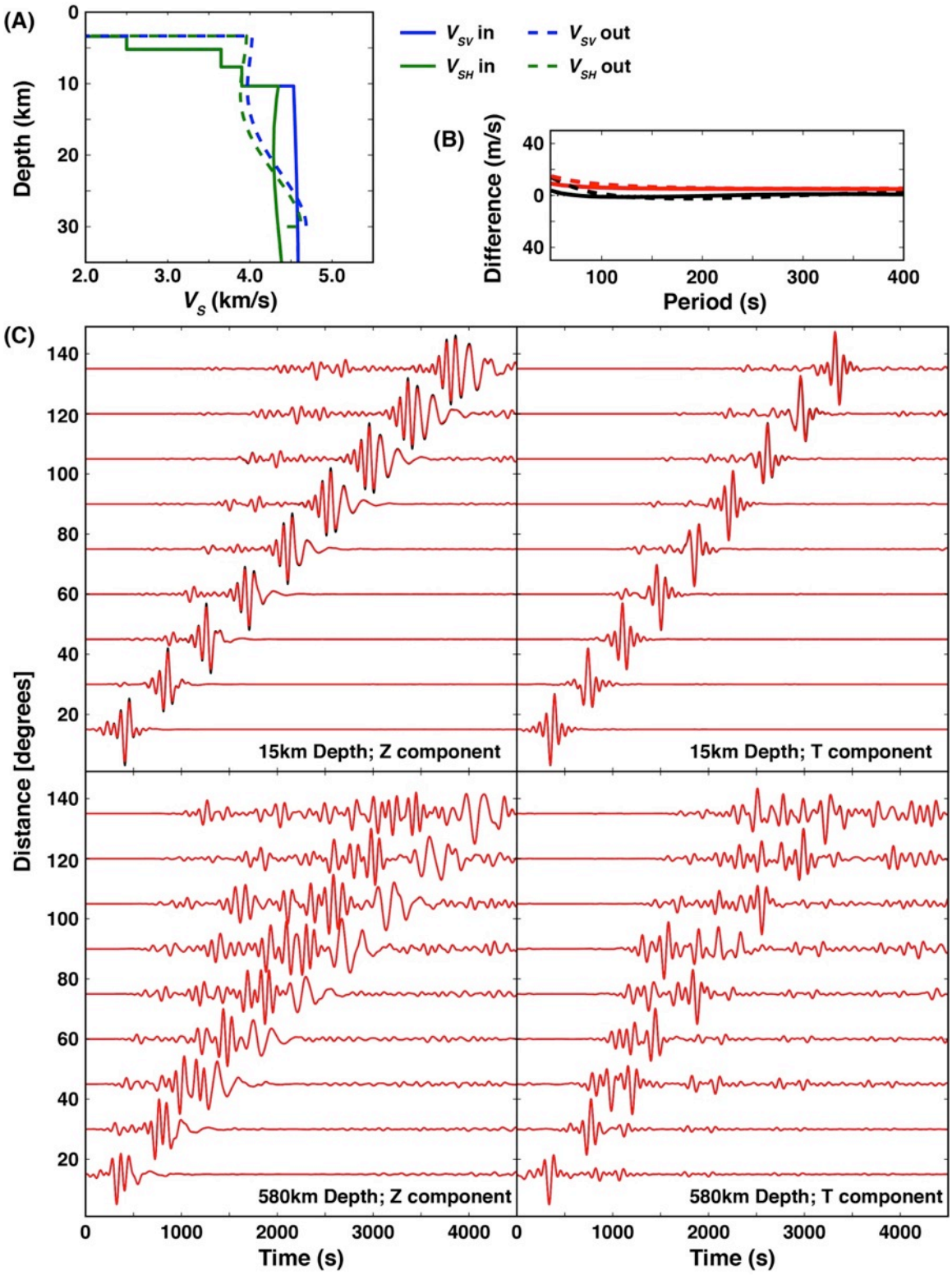

Fig. S2

Demonstration that long-period waveforms and surface-wave dispersion are unaffected by our parameterization of a smooth 30 km crustal layer derived for a synthetic "oceanic"

input structure using the two-step modeling scheme (Section S1.1): (A) layered synthetic input (continuous lines) and smooth 30 km output structures (broken lines); (B) long-period Love (red) and Rayleigh (black) fundamental-mode phase (solid) and group (dashed) velocity misfit between layered input and smooth output models; (C) vertical and transverse component long-period (60-400s) waveforms for shallow and deep events calculated in the layered input (black) and smooth output (red) models.

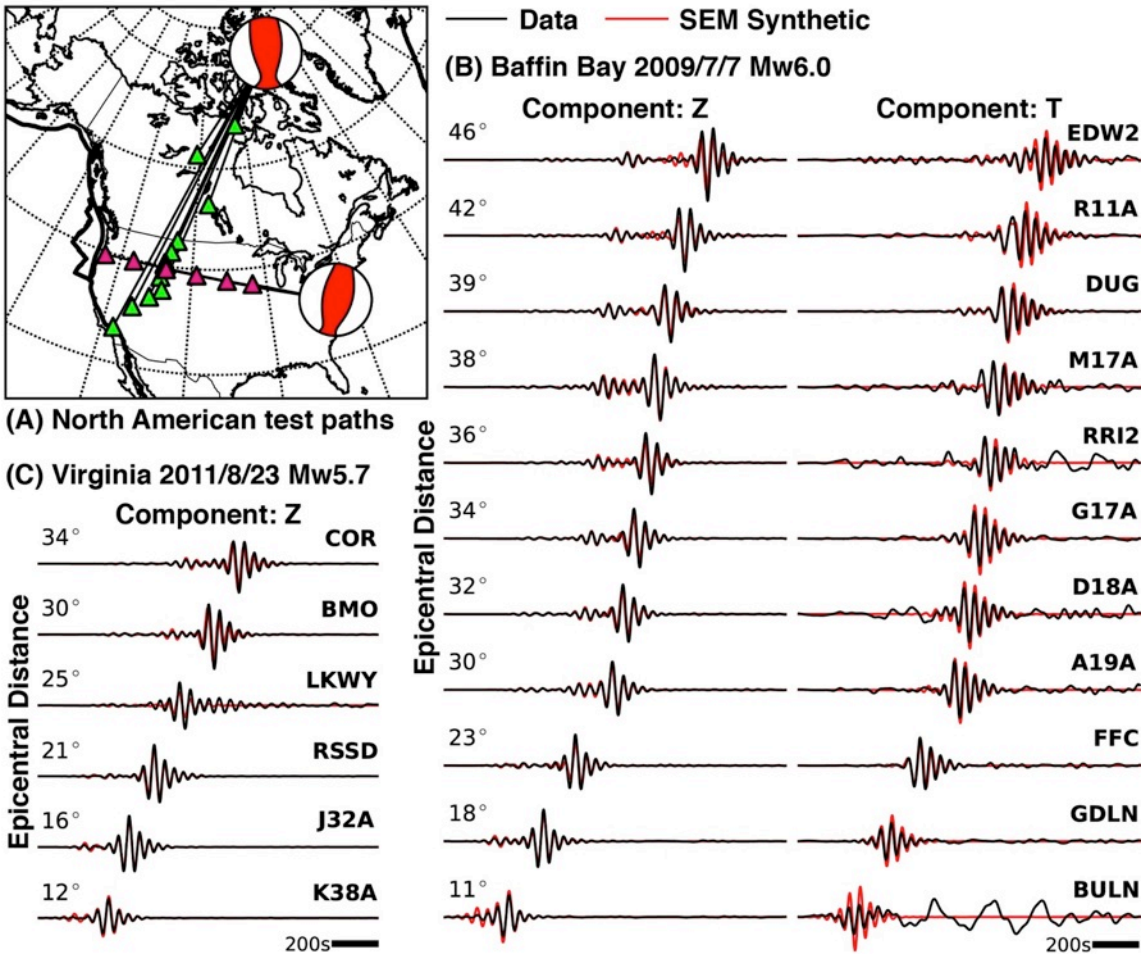
Data
SEM Synthetic
(A) North American test paths
(B) Baffin Bay 2009/7/7 Mw6.0
Component: Z
Component: T
Epicentral Distance
46°
42°
39°
38°
36°
34°
32°
30°
23°
18°
11°
EDW2
R11A
DUG
M17A
RRI2
G17A
D18A
A19A
FFC
GDLN
BULN
200s
(C) Virginia 2011/8/23 Mw5.7
Component: Z
Epicentral Distance
34°
30°
25°
21°
16°
12°
COR
BMO
LKWY
RSSD
J32A
K38A
200s

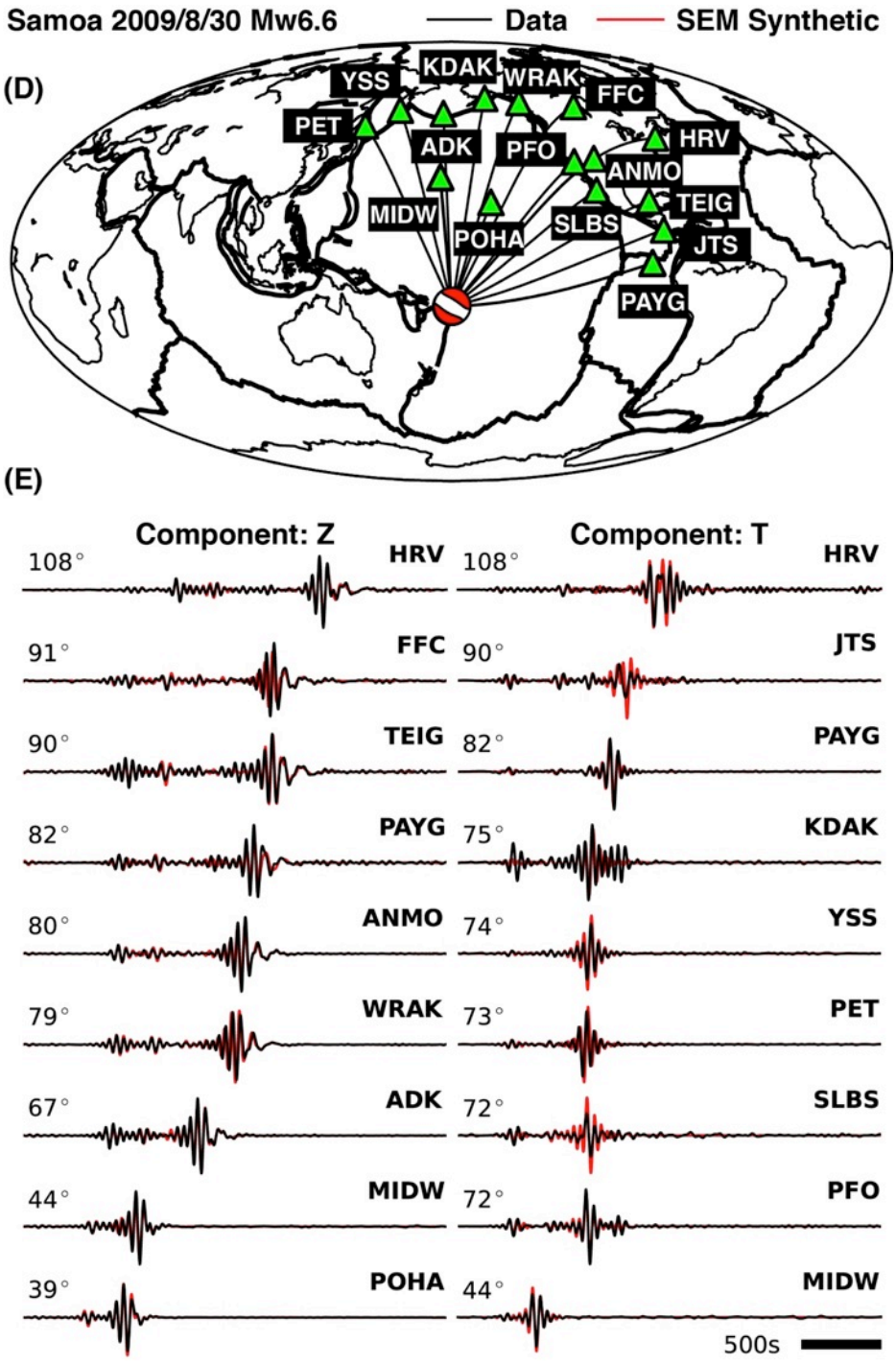

Fig. S3

Examples of waveform fits for events *not* included in our dataset and at periods shorter than used in our modeling (40s minimum period instead of 60s). Continental paths are featured in panels (A)-(C), while oceanic paths are shown in (D) and (E). In general, we observe very close fits between data and SEM synthetics in both settings, for both fundamental-mode and overtone wavetrains on vertical and transverse components (with the exception of station BULN, which exhibits high noise levels on the transverse

component in panel (B)). These results supply an important independent validation of the SEMum2 model.

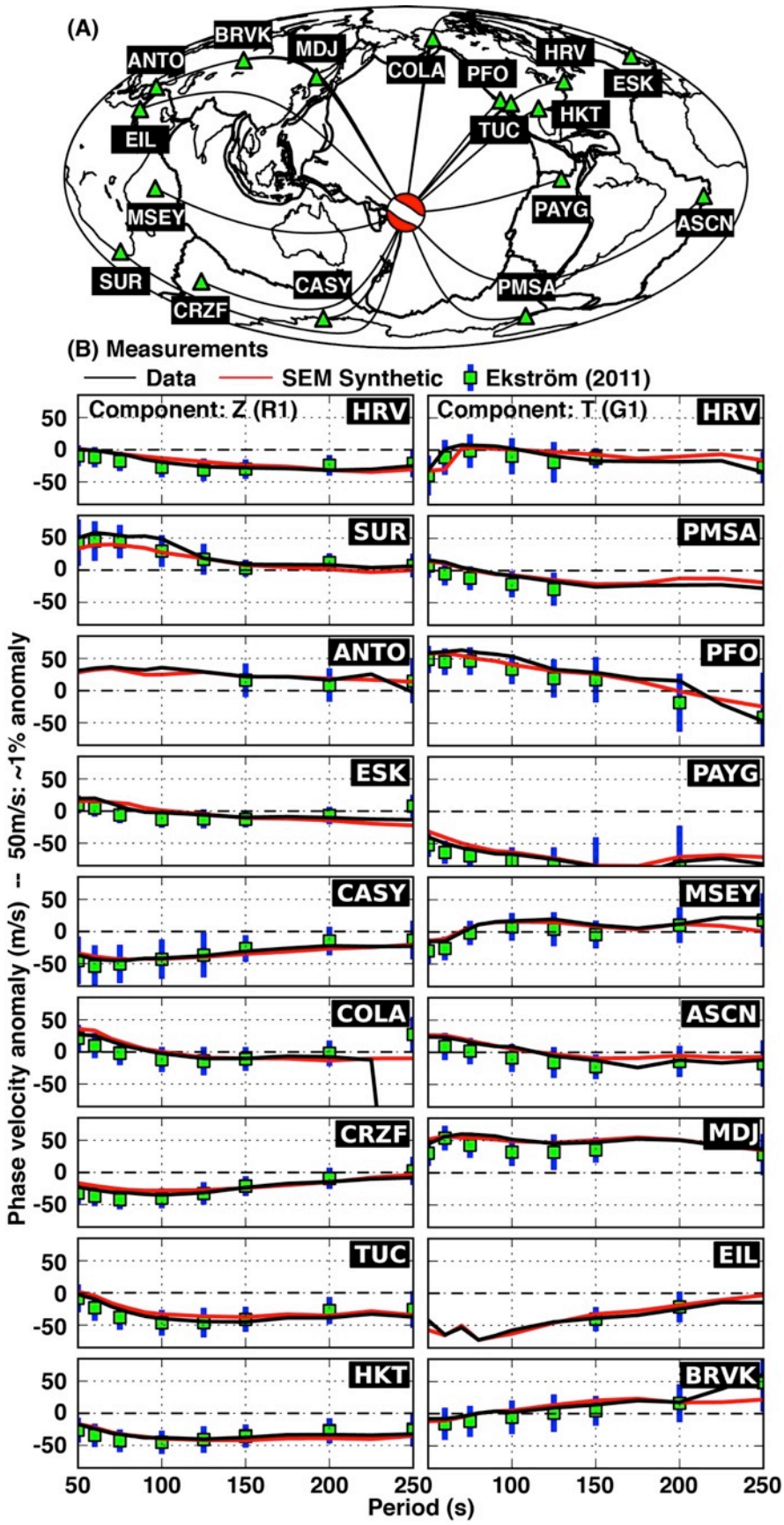
(A)
BRVK
ANTO
MDJ
COLA
HRV
PFO
ESK
HKT
TUC
EIL
PAYG
ASCN
MSEY
SUR
CASY
PMSA
CRZF
(B) Measurements
Data
SEM Synthetic
Ekström (2011)
Component: Z (R1)
Component: T (G1)
HRV
PMSA
SUR
PFO
ANTO
PAYG
ESK
MSEY
CASY
ASCN
COLA
MDJ
CRZF
EIL
TUC
BRVK
HKT
50
0
-50
Phase velocity anomaly (m/s) -- 50m/s: ~1% anomaly
50
100
150
200
250
Period (s)

Fig. S4

Comparisons between fundamental-mode phase velocities measured from waveform data and SEM synthetics for SEMum2 using the multitaper technique of (*45*) – again for an event not included in our inversion (Samoa 2009/8/30 Mw6.6), along a range of oceanic, continental, and mixed paths. Absolute phase-velocity anomalies are displayed with respect to the global 1D-mean reference model associated with SEMum2, for which 50m/s corresponds to an anomaly of 1-1.3% in the period range considered. Overall, we find excellent fits between measurements performed on data and SEM synthetics – consistent with the quality of waveform fits observed for SEMum2. Further, we also show phase velocities for the same event and paths inferred from the single-station phase-anomaly dataset of (*46*) (used to constrain the GDM52 dispersion model discussed therein). Where available, phase-velocity anomalies from (*46*) are in general compatible with our own measurements to within their published uncertainties. Panel (A): paths for which phase velocity measurements are available. Panel (B): phase-velocity measurements performed on data (black) and SEM synthetics (red) using the technique of (*45*), as well as those inferred from (*46*) with associated uncertainties (green squares, blue 2σ error-bars).

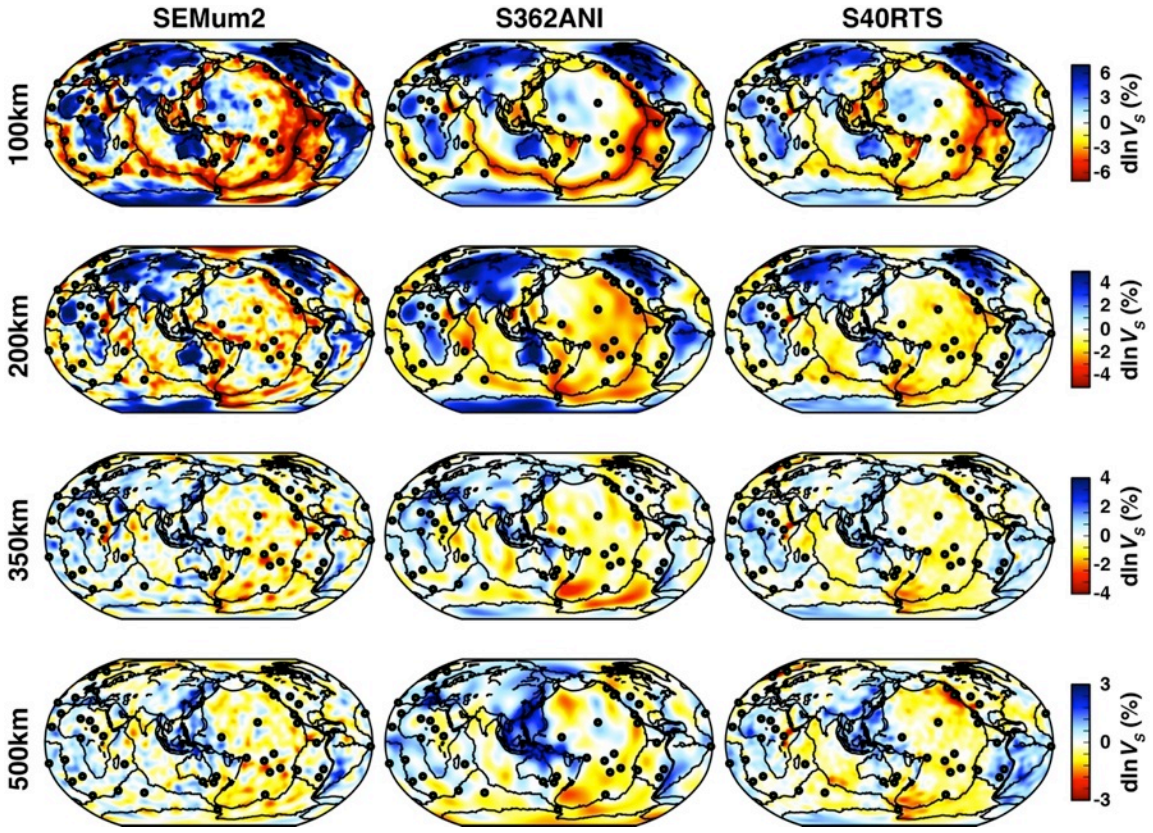

Fig. S5

Global isotropic V_S structure in the SEMum2 model, as well as two other recent global models – S362ANI (*47*) and S40RTS (*48*) – at a range of upper-mantle and transition zone depths. Model structure is plotted as variations (%) with respect to the 1D reference associated with each model. Circles denote hotspots of Steinberger (*30*). All three models agree well at long wavelengths, while SEMum2 in general exhibits stronger, more concentrated anomalies.

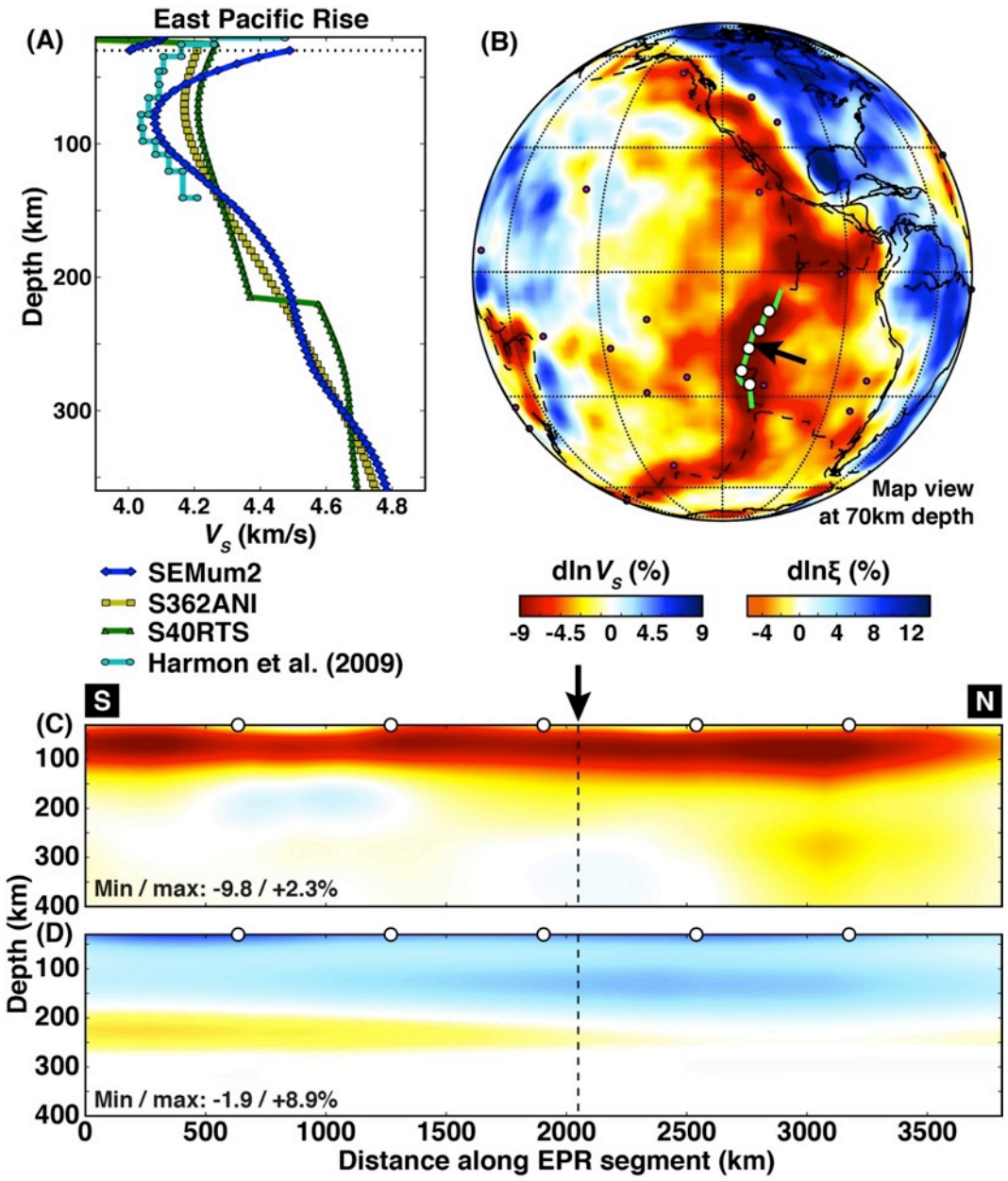

Fig. S6

Isotropic V_S structure in SEMum2 beneath the East Pacific Rise (EPR). In panel (A): a comparison between the mean 1D V_S profile obtained from the high-resolution OBS-based tomographic study of EPR structure by (*49*), with that sampled from global models SEMum2, S362ANI (*47*), and S40RTS (*48*), in the same location. The 1D profile of the Harmon et al. study was obtained from a harmonic mean of the central portion of their model over length-scales consistent with the a priori correlation lengths employed in the SEMum2 inversion (~400 km). It is immediately clear that SEMum2 more-closely recovers the strength and depth of the low-velocity zone (LVZ) beneath the EPR inferred from the local study than either of the other global models. Panel (B): Relative variations in isotropic V_S structure at 70 km depth in SEMum2, focused on the EPR, showing both

the location of the comparison in (A) (black arrow) and the extent of the ~3750 km line of section in (C) (portion of EPR highlighted in green). Panels (C) and (D): a cross section following the portion of the EPR shown in (B), illustrating the strength and extent of the strong low-velocity anomaly imaged beneath the EPR in SEMum2 (C), nearly -10%, as well as the pronounced reduced $\xi=V_{SH}^2/V_{SV}^2$ signal (D), interpreted as enhanced vertical flow beneath the ridge (see also Figure S12). Black arrow and dashed line indicate approximate location of profiles in (A).

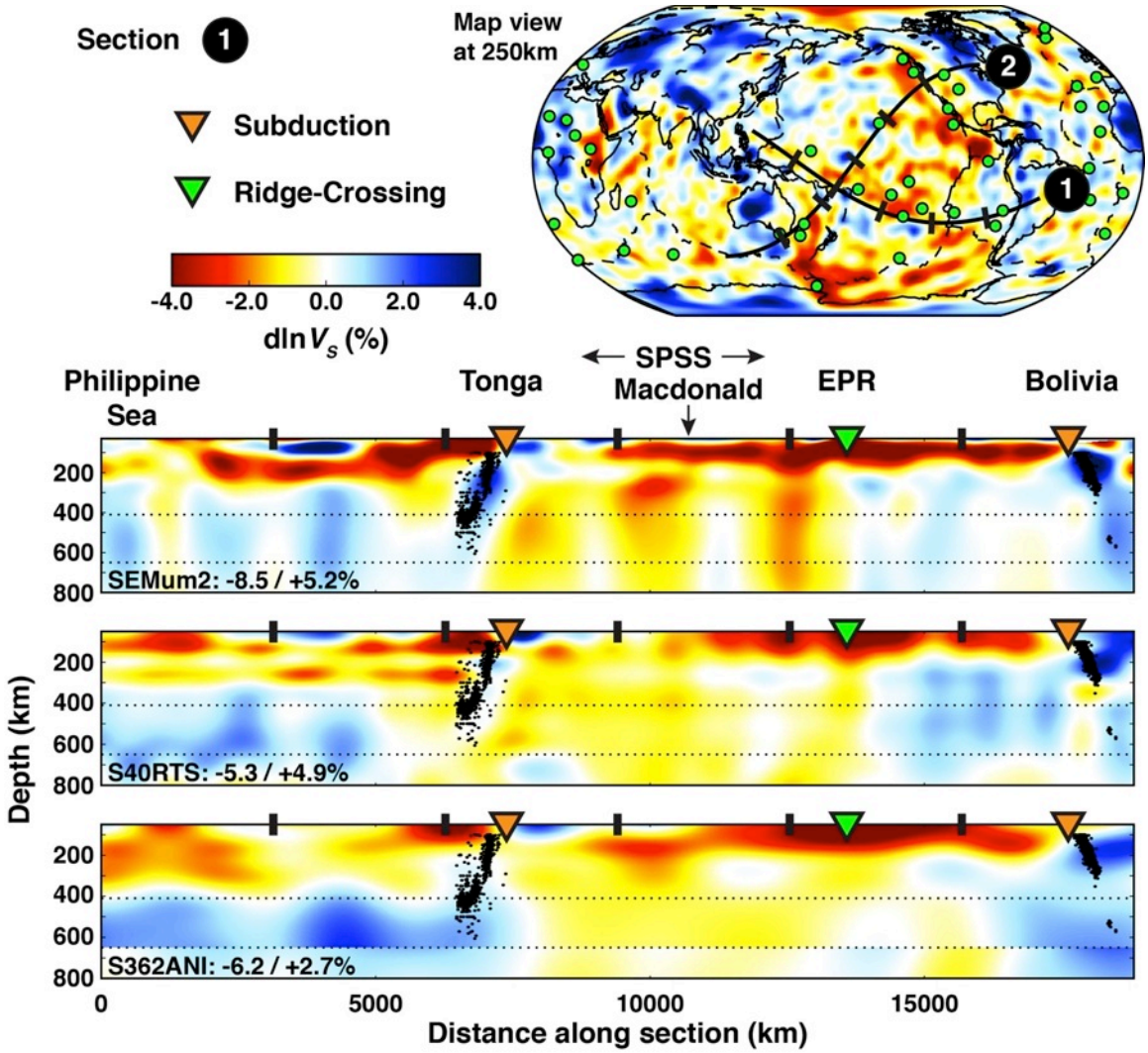

Fig. S7

Cross sections showing relative variations in isotropic V_S structure across the Pacific, corresponding to path (1) (WNW-to-ESE) on the accompanying map. Upper section: SEMum2; middle section: S40RTS (*48*); bottom section: S362ANI (*47*). Inverted triangles in green denote ridges crossing the line of section, while those in orange correspond to subduction zones (earthquake hypocenters also shown, highlighting subducted slabs). Maximum positive and negative V_S perturbation for each model (relative to their own respective 1D reference) is also indicated (inset). Large-scale patterns of V_S structure are clearly compatible between the three models, though SEMum2 recovers stronger lateral heterogeneity – particularly in the LVZ – as well as a more-continuous signature of high velocities associated with subducted slabs and low-velocity "conduits" beneath the South-Pacific Superswell (*12*). Abbreviations: SPSS – Pacific Superswell. Green circles in map view correspond to hotspot locations of Steinberger (*30*).

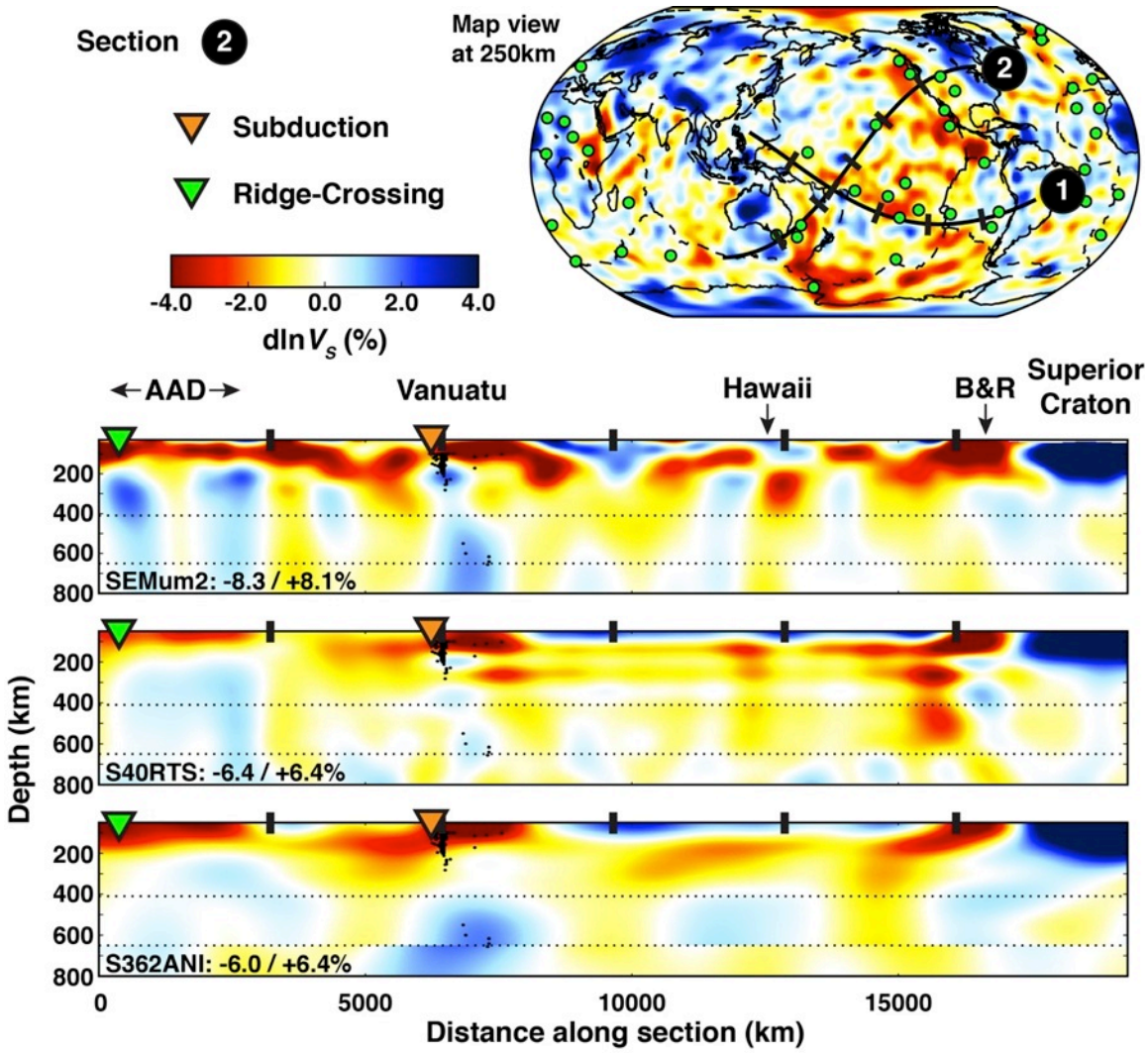

Fig. S8

Similar to Figure S7, but now showing relative variations in isotropic V_S corresponding to path (2) (SW-to-NE). Again, large-scale patterns of structure are consistent across models, while SEMum2 exhibits stronger heterogeneity. Abbreviations: AAD – Australian-Antarctic Discordance (*59*); B&R – Basin and Range.

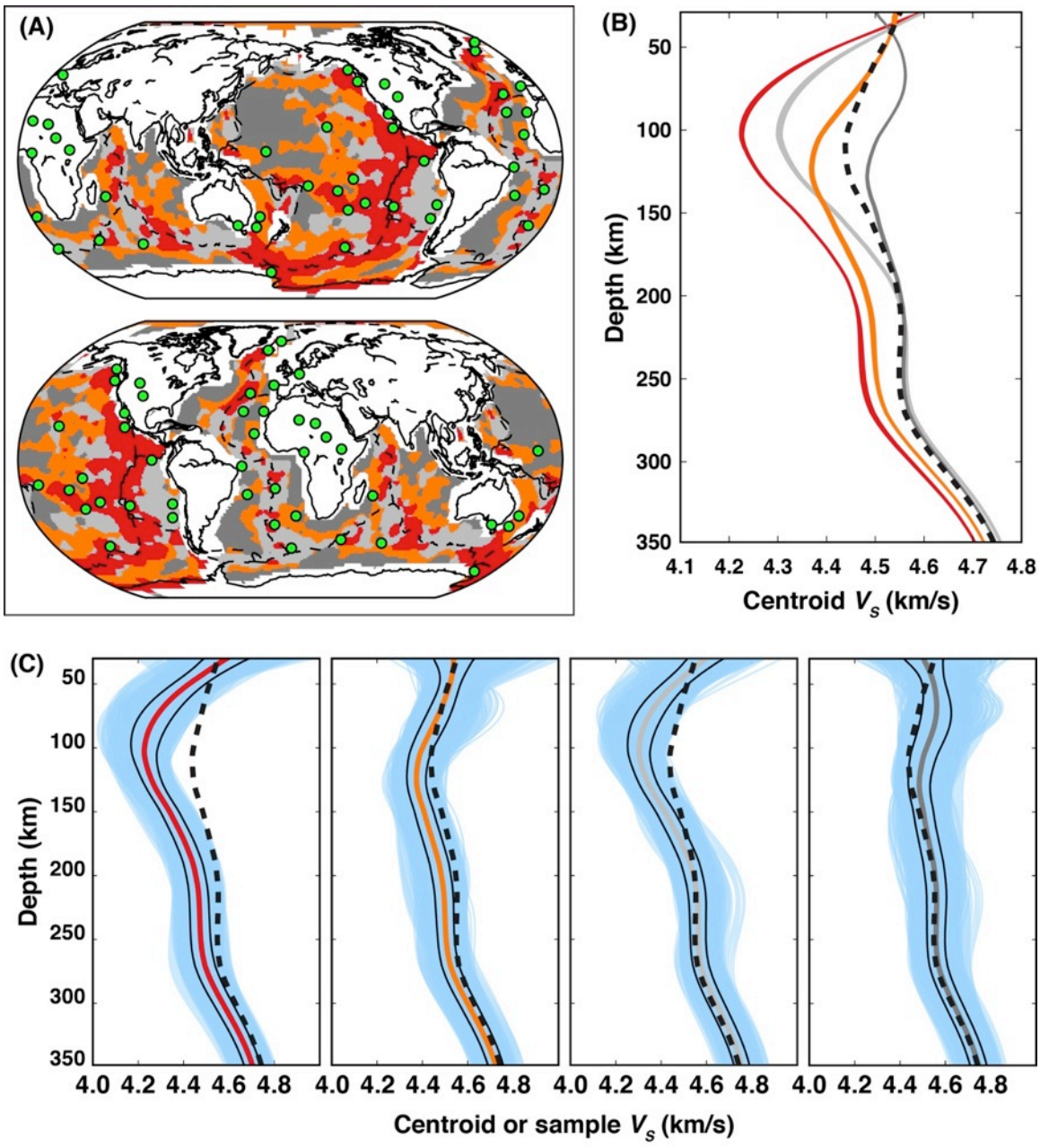

Fig. S9

Detailed cluster analysis of SEMum2 isotropic V_S structure in the oceanic upper mantle (30-350 km depth) using the k-means algorithm (*50*) (4 clusters). Panel (A): lateral extent of the resulting 4 classes of oceanic V_S structure in both Pacific and Atlantic Ocean-centered views. Green circles denote hotspots of Steinberger (*30*). Panel (B): ensembles of mean 1D V_S models for the 4 classes shown in (A) using an identical color scheme, along with the global 1D-mean for comparison (black, dashed). Ensembles of means reflect model uncertainties obtained in the bootstrap resampling analysis (Section S4.2), as noted in Section S3. For the mean profile associated with each class of structure, we again note the presence of a strong V_S gradient (150-200 km) above almost constant V_S (200-350 km), as found in early models of the oceanic upper-mantle (*60*). Panel (C):

populations of 1D V_S models sampled from SEMum2 that fall into each of the 4 clusters (light blue, background), overlain by the corresponding cluster-mean profiles and the global mean (black, dashed) – black lines correspond to +/- 1σ variation around the cluster mean within each population.

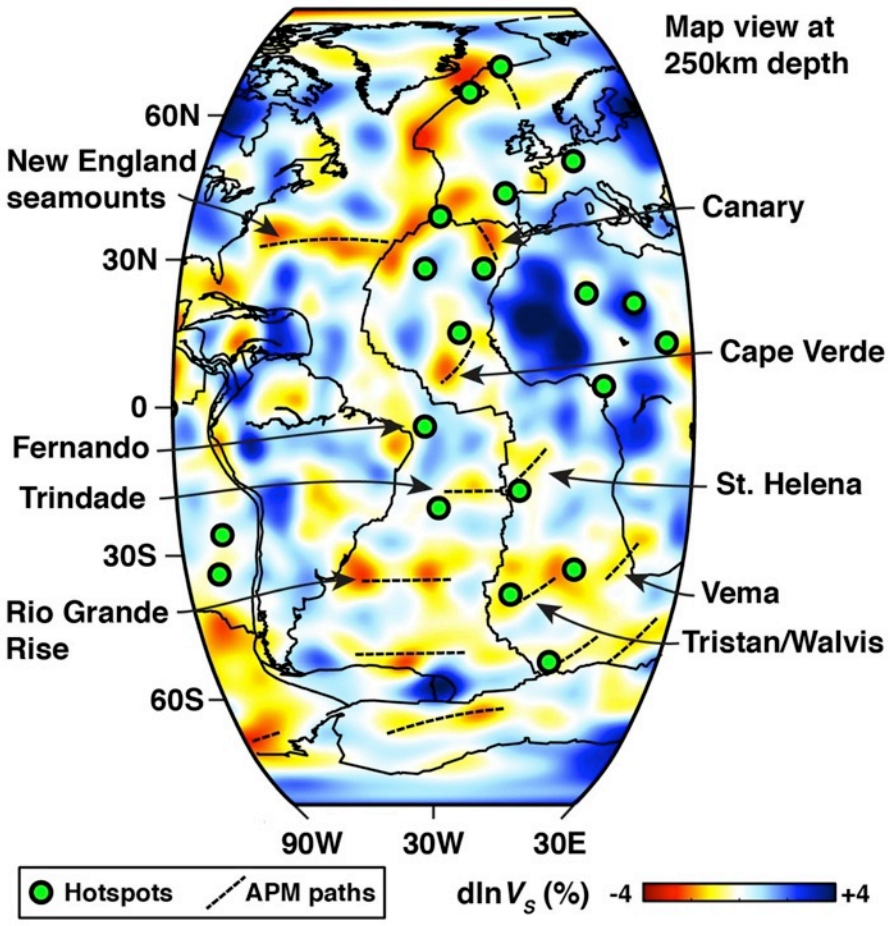

Fig. S10

Atlantic Ocean centered view of SEMum2 V_S variations (w.r.t. the global mean) at 250 km depth, demonstrating preferential alignment between Atlantic LVFs and the APM of (*14*) (broken lines). LVF orientations often correlate with Atlantic hotspot tracks and seamount chains, as labeled, including those referred to in the main text. Further, we note impressive recovery of the high-velocity signature of the South-Sandwich Islands subduction zone at ~60°S. Green circles denote hotspots of Steinberger (*30*).

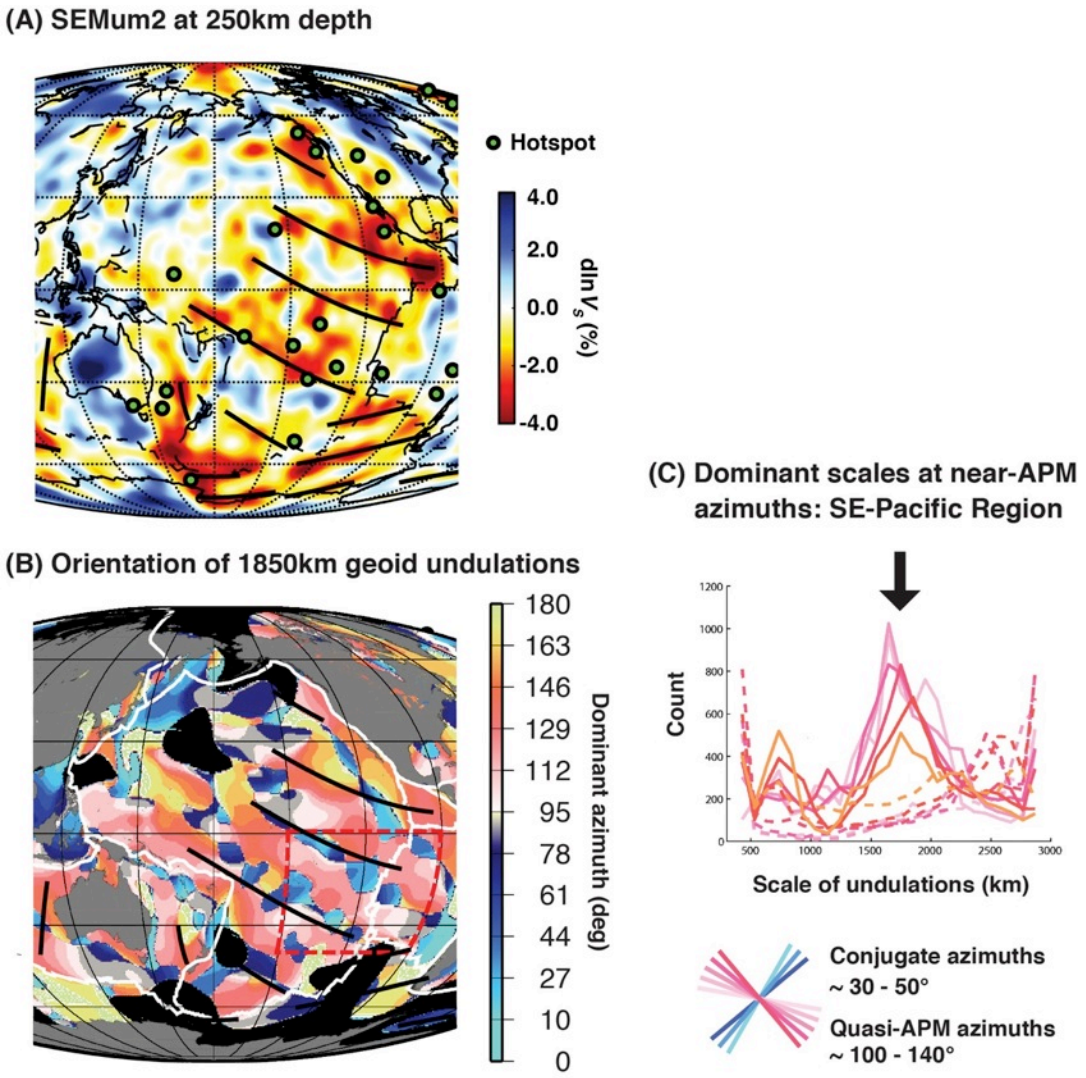

Fig. S11

Comparison between SEMum2 Pacific LVFs and the directional wavelet analysis of the EGM2008 geoid by Hayn et al. (*15*). Panel (A): SEMum2 V_S structure at 250 km depth, focused on the Pacific, with APM paths (*14*) overlain as in Fig. 2 of the main text. We note that the approximate 2000 km spacing between the Pacific LVFs is closer to ~1900 km when limited specifically to the SE Pacific region. Green circles – hotspots (*30*). Panel (B): modified from Hayn et al. (*15*, reproduced with permission of the authors) – azimuth of dominant orientation of geoid undulations at 1850 km wavelength. As noted, pink colors correspond to quasi-APM azimuths in the central/eastern Pacific, while blue colors correspond to the conjugate direction. Intriguingly, the LVFs appear to fall between the APM-parallel lineations in the geoid at the 1850 km scale – an observation that we expand upon in Section S5.3. Panel (C): modified from Hayn et al. (*15*, reproduced with permission of the authors) – histograms of dominant wavelengths of geoid undulations (solid lines) and predicted bathymetric effect on the geoid (dashed lines) for the SE Pacific region (red dashed box in Panel (B)) at quasi-APM azimuths. A

clear peak (black arrow) is seen at a mean wavelength of ~1900 km that appears independent of the bathymetric signal (*15*).

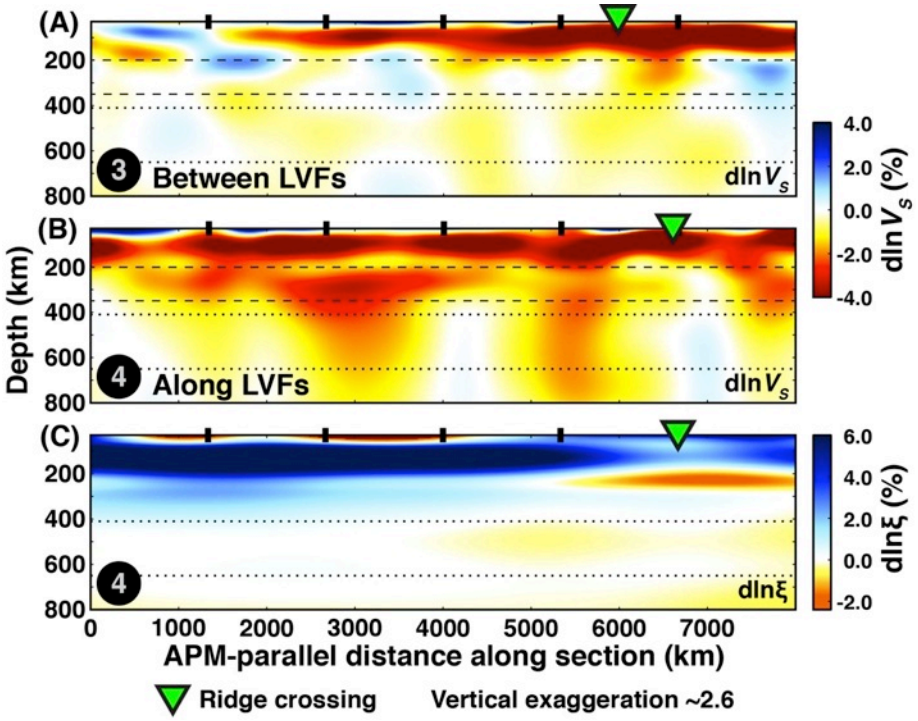

Fig. S12

Depth cross-sections through SEMum2, along profiles *parallel* to APM (*14*) that are identical to those in Figure 3 of the main text (profiles 3 and 4), but now extending to 800 km depth. Refer to Figure 3A for profile locations. Panels (A) and (B): relative variations in isotropic V_S along profiles 3 and 4; Panel (C): variations in the radial anisotropy parameter $\xi=V_{SH}^2/V_{SV}^2$ along profile 4 – the same profile as in panel (B). Profile (A) is located between LVFs, while profile (B) is within an LVF.

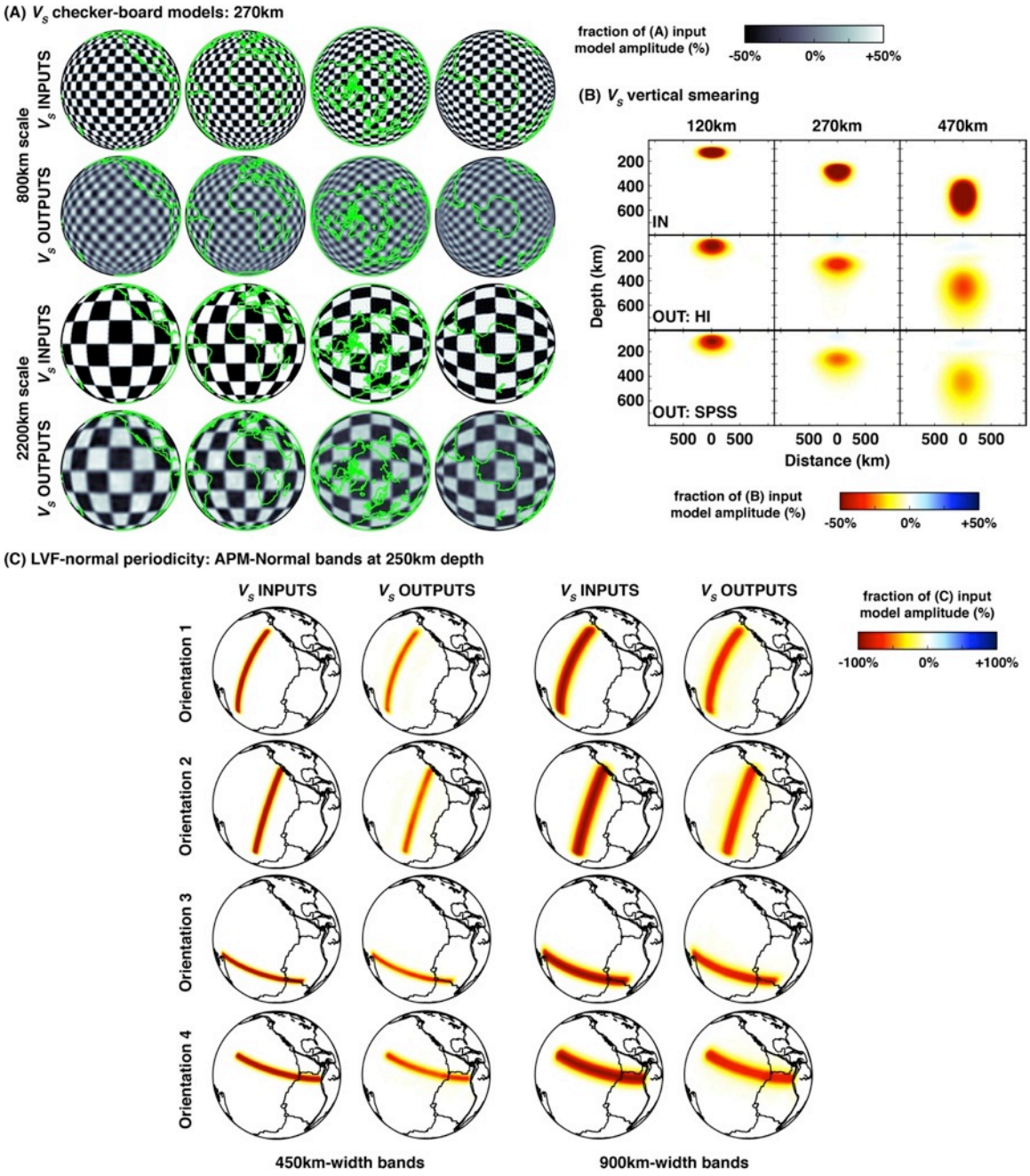

Fig. S13

Linear resolution analysis for the isotropic V_S portion of the SEMum2 model, focused on both global and central/eastern Pacific structure. Panel (A): global checkerboard test models at 270 km depth with ~800 km and ~2200 km maximum block widths for both equatorial and polar orientations. Both scales are well retrieved, with no indication of ray-like smearing or gaps in sensitivity, even at the poles. Panel (B): isolated point perturbations (~2° width) at 120, 270, and 470 km depth – inputs shown in the top row, structure retrieved with inputs located beneath Hawaii (high-density data coverage) and the Pacific Superswell (lower-density) shown in the middle and bottom row, respectively. Though amplitudes are not honored, we note good recovery of the morphology of input

structures at both locations, with little evidence of vertical smearing. Panel (C): band-like input structures (200-350 km depth) with ~450 km and ~900 km widths oriented normal (**1**,**2**) and parallel (**3**,**4**) to APM (*14*). The homogeneous nature of the input bands is honored in the retrieved APM-normal structure, indicative that the ~2000 km APM-normal periodicity of Pacific LVFs is not the result of poor data coverage or model parameterization. Both scales of APM-parallel input bands are retrieved, indicating that the widths of the Pacific LVFs are well resolved. Color scales chosen to highlight deficiencies in the resolution of our model: panels (A) and (B) saturate at 50% of the input level in order to emphasize low-amplitude smearing artifacts (lateral or vertical, respectively), while panel (C) saturates at 100% of the input level to emphasize gaps in coverage that could artificially give rise to the APM-normal periodicity or lead to poor recovery of the narrow APM-parallel test structures (otherwise difficult to detect if over saturated).

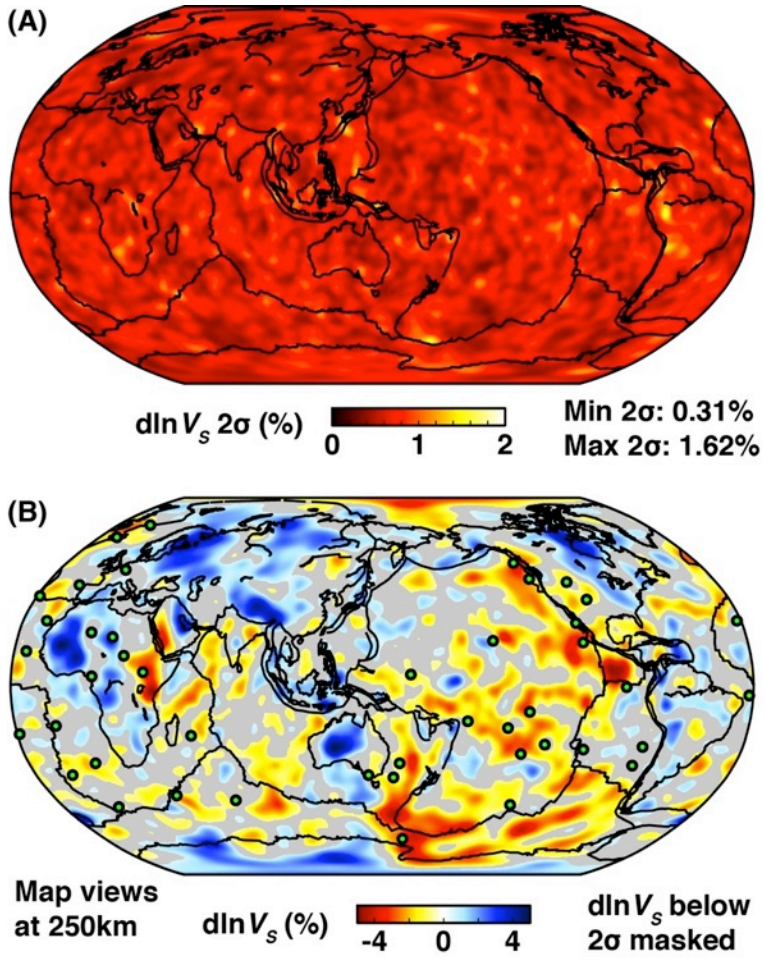

Fig. S14

Results of the bootstrap resampling analysis (Section S4.2), here featured at LVF depths (250 km). Panel (A): 2σ uncertainties (% dlnV_S) from 20 bootstrap iterations, shown in global map view. Panel (B): relative variations in V_S structure at 250 km, shown in the same view, but with perturbation amplitudes below local 2σ in (A) masked. Given the uncertainty estimates obtained here, it is clear that the LVF structures remain significant at the 2σ level.

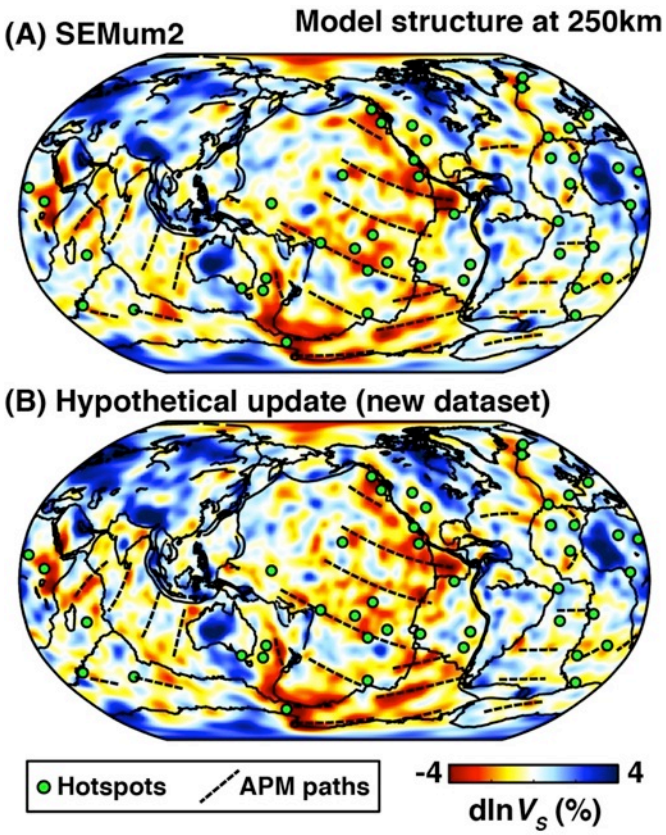

Fig. S15

Comparison between SEMum2 model structure at LVF depths (250 km) – similar to Figure 2 in the main text – shown in panel (A), and that obtained from a hypothetical model update using a new independent waveform dataset (Section S4.3), in panel (B). As noted in the text, the model update scheme requires structure to adjust rapidly, if required by the data. We observe that SEMum2 structure at 250 km depth remains stable following the update step, with the LVFs remaining a prominent feature. Further, both models correlate at R>0.9 (up to spherical harmonic degree 48) at all depths throughout the upper mantle. Also shown: hotspot locations (green circles) (*30*); APM (black dashed) (*14*).

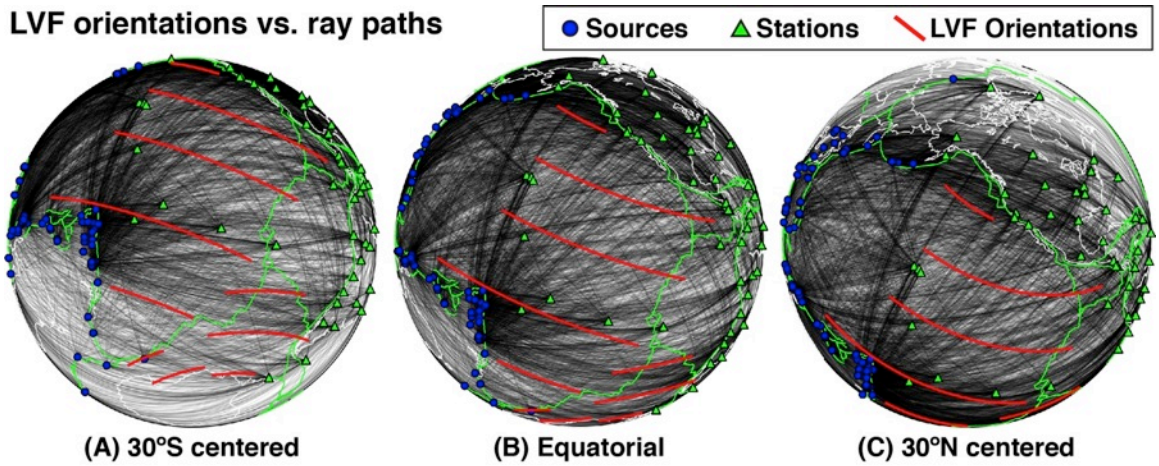

Fig. S16

Comparisons between Pacific and West-Antarctic LVF orientations (APM (*14*) paths from Figure 2 in the main text) and a sparse, but representative subset of rays traversing the region from Western-Pacific and Arctic sources to Western Hemisphere and ocean-island receivers (Section S4.4). Maps shown with 30°S (A), equatorial (B), and 30°N-centered (C) views; sources and stations shown as blue circles and green triangles, respectively. It is immediately clear that the LVFs cannot correspond to ray paths, confirming in practice that the alignment of the LVFs with APM is not an artifact of the path coverage.

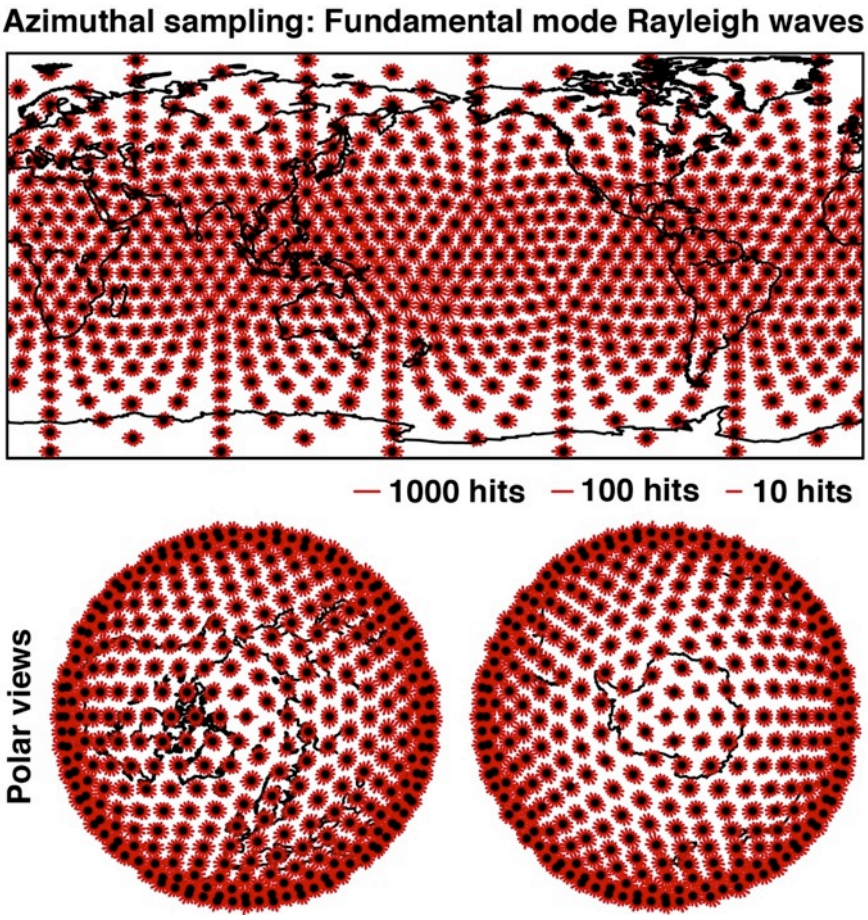

Fig. S17

Rose diagrams demonstrating homogeneity of azimuthal coverage for the fundamental-mode Rayleigh wave portion of our waveform dataset. Homogeneity of coverage, such as that shown here, is crucial for avoiding tradeoffs between isotropic velocity variations and azimuthal anisotropy.

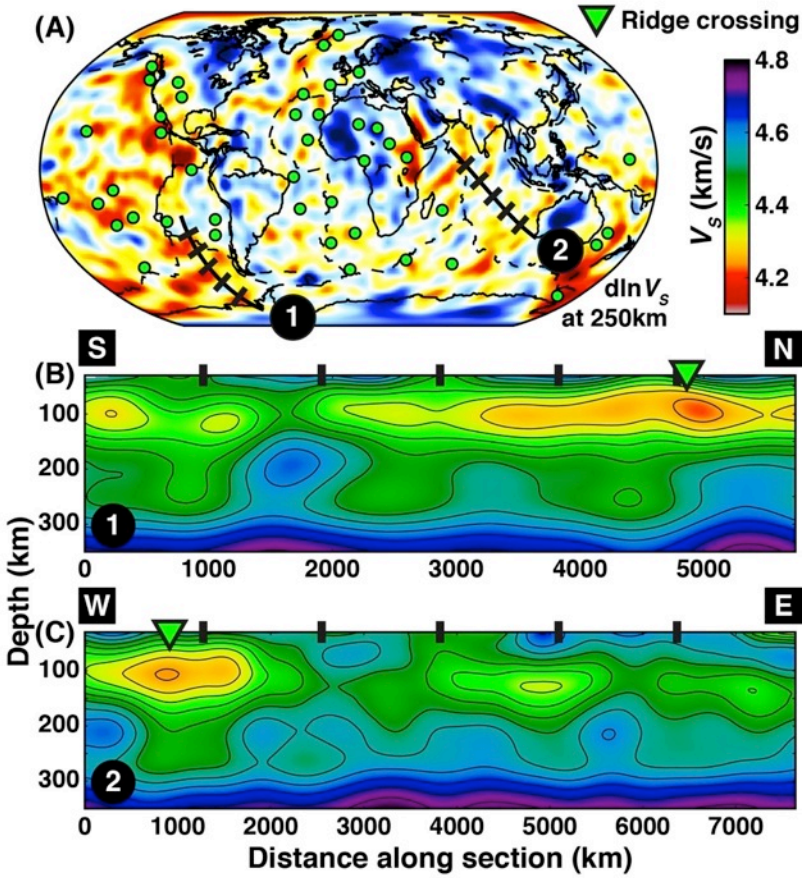

Fig. S18

Absolute V_S cross-sections perpendicular to APM (*14*) in the upper 350 km of the mantle for paths shown in map view in panel (A): panel (B) – beneath the Antarctic Plate; panel (C) – beneath the Indian Plate. As in Figure 3 in the main text, the vertical velocity gradient at the base of the LVZ is considerably stronger in regions between LVFs than where LVFs are present, even beneath the slow-moving Antarctic plate. Overlain contour interval: 50m/s.

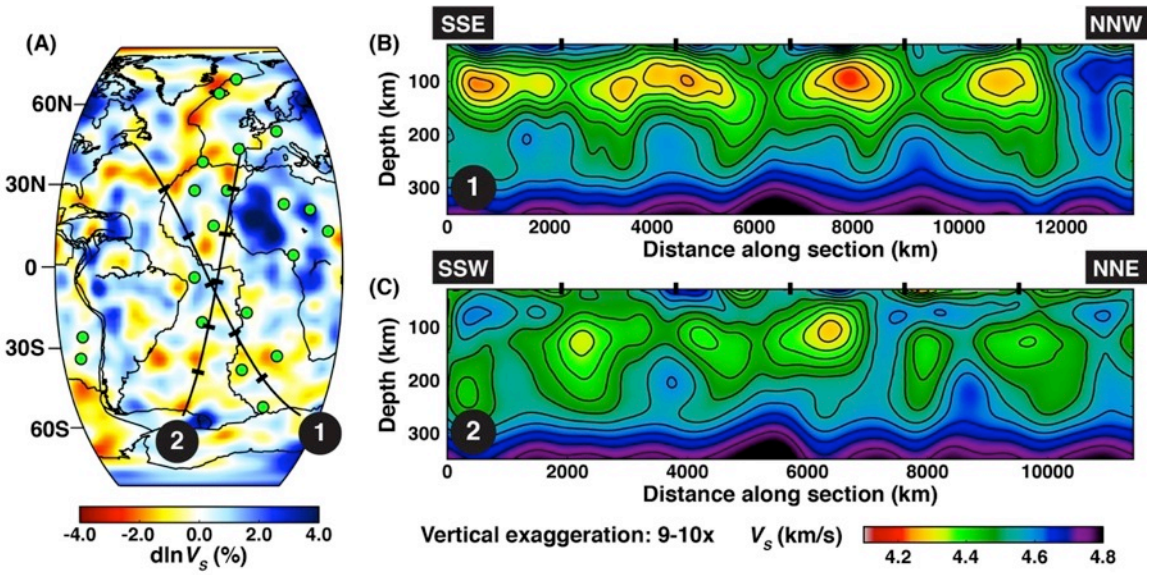

Fig. S19

Absolute V_S cross-sections in the upper 350 km of the Atlantic upper mantle for paths shown in map view in panel (A) (dlnV_S at 250 km depth). The nature of Atlantic APM (e.g. Fig. S10) makes it difficult to consistently remain quasi-perpendicular to APM on such long profiles, however those shown above attempt to do so on average (path (1) in panel (B) for its entire length, path (2) in panel (C) until ~6500 km along section). Especially panel (B), but also in the quasi-APM-normal portion of panel (C), the LVF structures are immediately apparent – particularly their ~2000 km periodicity and depth extent beyond the base of the classical LVZ. Overlain contour interval: 50m/s.

Table S1.

Final-iteration waveform variance-reduction for SEMum2, and associated numbers of accepted waveform windows / data points (bracketed), listed by component and windowed-wavetrain type. Over 99,000 waveform windows, corresponding to more than 5,200,000 data points, are accepted into the final inversion iteration. Here, variance reduction is defined in percent of one minus the squared 2-norm of the residual between the data and synthetics normalized by that of the data: 100 x [1 - $||\mathbf{d} - \mathbf{g}(\mathbf{m})||^2 / ||\mathbf{d}||^2$].

	Fundamental	Overtone	Mixed
L	68.1% [7,964 / 428,700]	80.9% [14,475 / 913,434]	74.9% [3,434 / 219,187]
T	77.3% [13,438 / 509,014]	71.2% [14,640 / 511,837]	82.2% [4,596 / 232,885]
Z	69.9% [13,562 / 731,590]	79.5% [22,296 / 1,341,729]	77.6% [4,951 / 313,140]

References and Notes

1. V. Lekic, S. Cottaar, A. M. Dziewonski, B. Romanowicz, Cluster analysis of global lower mantle tomography: A new class of structure and implications for chemical heterogeneity. *Earth Planet. Sci. Lett.* **357-358**, 68–77 (2012). doi:10.1016/j.epsl.2012.09.014

2. M. Richards, D. Engebretson, Large-scale mantle convection and the history of subduction. *Nature* **355**, 437–440 (1992). doi:10.1038/355437a0

3. A. Davaille, E. Stutzmann, G. Silveira, J. Besse, V. Courtillot, Convective patterns under the Indo-Atlantic " box ". *Earth Planet. Sci. Lett.* **239**, 233–252 (2005). doi:10.1016/j.epsl.2005.07.024

4. B. Romanowicz, Y. C. Gung, Superplumes from the core-mantle boundary to the lithosphere: implications for heat flux. *Science* **296**, 513–516 (2002). doi:10.1126/science.1069404 Medline

5. W. J. Morgan, Convection Plumes in the Lower Mantle. *Nature* **230**, 42–43 (1971). doi:10.1038/230042a0

6. F. Rickers, A. Fichtner, J. Trampert, Imaging mantle plumes with instantaneous phase measurements of diffracted waves. *Geophys. J. Int.* **190**, 650–664 (2012). doi:10.1111/j.1365-246X.2012.05515.x

7. F. M. Richter, B. Parsons, On the interaction of two scales of convection in the mantle. *J. Geophys. Res.* **80**, 2529–2541 (1975). doi:10.1029/JB080i017p02529

8. G. Nolet, F. A. Dahlen, Wave front healing and the evolution of seismic delay times. *J. Geophys. Res.* **105**, (B8), 19043–19054 (2000). doi:10.1029/2000JB900161

9. C. Tape, Q. Liu, A. Maggi, J. Tromp, *Geophys. J. Int.* **160**, 195–216 (2010).

10. A. Fichtner, B. L. N. Kennet, H. Igel, H.-P. Bunge, Full seismic waveform tomography for upper-mantle structure in the Australasian region using adjoint methods. *Geophys. J. Int.* **179**, 1703–1725 (2009). doi:10.1111/j.1365-246X.2009.04368.x

11. V. Lekić, B. Romanowicz, Inferring upper-mantle structure by full waveform tomography with the spectral element method. *Geophys. J. Int.* **185**, 799–831 (2011a). doi:10.1111/j.1365-246X.2011.04969.x

12. M. K. McNutt, K. M. Fischer, in *Seamounts, Islands and Atolls, Geophys. Monogr. Ser*. **43**, B. H. Keating, *et al.*, Eds. (AGU, Washington D. C., 1987) 25-34.

13. V. Lekic, B. Romanowicz, Tectonic regionalization without a priori information: A cluster analysis of upper mantle tomography. *Earth Planet. Sci. Lett.* **308**, 151–160 (2011b). doi:10.1016/j.epsl.2011.05.050

14. C. Kreemer, Absolute plate motions constrained by shear wave splitting orientations with implications for hot spot motions and mantle flow. *J. Geophys. Res.* **114**, (B10), B10405 (2009). doi:10.1029/2009JB006416

15. M. Hayn, I. Panet, M. Diament, M. Holschneider, M. Mandea, A. Davaille, Wavelet-based directional analysis of the gravity field: evidence for large-scale undulations. *Geophys. J. Int.* **189**, 1430–1456 (2012). doi:10.1111/j.1365-246X.2012.05455.x

16. R. Katzman, L. Zhao, T. H. Jordan, High-resolution, two-dimensional vertical tomography of the central Pacific mantle using *ScS* reverberations and frequency-dependent travel times. *J. Geophys. Res.* **103**, 17933–17971 (1998). doi:10.1029/98JB00504

17. L. Colli, A. Fichtner, H.-P. Bunge, *Tectonophysics*. Published online 27 June 2013. 10.1016/j.tecto.2013.06.015

18. C. J. Wolfe, S. C. Solomon, G. Laske, J. A. Collins, R. S. Detrick, J. A. Orcutt, D. Bercovici, E. H. Hauri, Mantle P-wave velocity structure beneath the Hawaiian hotspot. *Earth Planet. Sci. Lett.* **303**, 267–280 (2011). doi:10.1016/j.epsl.2011.01.004

19. G. Laske, A. Markee, J. A. Orcutt, C. J. Wolfe, J. A. Collins, S. C. Solomon, R. S. Detrick, D. Bercovici, E. H. Hauri, Asymmetric shallow mantle structure beneath the Hawaiian Swell-evidence from Rayleigh waves recorded by the PLUME network. *Geophys. J. Int.* **187**, 1725–1742 (2011). doi:10.1111/j.1365-246X.2011.05238.x

20. J. M. O'Connor, W. Jokat, A. P. le Roex, C. Class, J. R. Wijbrans, S. Keßling, K. F. Kuiper, O. Nebel, Hotspot trails in the South Atlantic controlled by plume and plate tectonic processes. *Nat. Geosci.* **5**, 735–738 (2012). doi:10.1038/ngeo1583

21. D. Snyder, S. Tait, *J. Fluid Mech.* **369**, 1–21 (1998).

22. J. Phipps Morgan, W. J. Morgan, Y.-S. Zhang, W. H. F. Smith, Observational hints for a plume-fed, suboceanic asthenosphere and its role in mantle convection. *J. Geophys. Res.* **100**, (B7), 12,753–12,767 (1995). doi:10.1029/95JB00041

23. N. Harmon, D. W. Forsyth, D. S. Weeraratne, Y. Yang, S. C. Webb, Mantle heterogeneity and off axis volcanism on young Pacific lithosphere. *Earth Planet. Sci. Lett.* **311**, 306–315 (2011). doi:10.1016/j.epsl.2011.09.038

24. D. R. Toomey, W. S. D. Wilcock, J. A. Conder, D. W. Forsyth, J. D. Blundy, E. M. Parmentier, W. C. Hammond, Asymmetric mantle dynamics in the MELT region of the East Pacific Rise. *Earth Planet. Sci. Lett.* **200**, 287–295 (2002). doi:10.1016/S0012-821X(02)00655-6

25. J. K. Hillier, A. B. Watts, “Plate-like” subsidence of the East Pacific Rise–South Pacific superswell system. *J. Geophys. Res.* **109**, B10102 (2004). doi:10.1029/2004JB003041

26. M. D. Ballmer, C. P. Conrad, E. I. Smith, N. Harmon, Non-hotspot volcano chains produced by migration of shear-driven upwelling toward the East Pacific Rise. *Geology* **41**, 479–482 (2013). doi:10.1130/G33804.1

27. T. Höink, A. Lenardic, M. Richards, Depth-dependent viscosity and mantle stress amplification: implications for the role of the asthenosphere in maintaining plate tectonics. *Geophys. J. Int.* **191**, 30–41 (2012). doi:10.1111/j.1365-246X.2012.05621.x

28. M. D. Ballmer, J. van Hunen, G. Ito, T. A. Bianco, P. J. Tackley, Intraplate volcanism with complex age-distance patterns: A case for small-scale sublithospheric convection. *Geochem. Geophys. Geosyst.* **10**, GC002386 (2009). doi:10.1029/2009GC002386

29. A. W. Hofmann, in *Treatise on Geophysics*, G. Schubert *et al*., Eds. (Elsevier, New York, 2007), vol. 2, chap. 3.

30. B. Steinberger, Plumes in a convecting mantle: Models and observations for individual hotspots. *J. Geophys. Res.* **105**, 11,127–11,152 (2000). doi:10.1029/1999JB900398

31. D. Komatitsch, J.-P. Vilotte, *Bull. Seismol. Soc. Am.* **88**, 368–392 (1998).

32. G. E. Backus, Long-wave elastic anisotropy produced by horizontal layering. *J. Geophys. Res.* **67**, 4427–4440 (1962). doi:10.1029/JZ067i011p04427

33. Y. Capdeville, J.-J. Marigo, Second order homogenization of the elastic wave equation for non-periodic layered media. *Geophys. J. Int.* **170**, 823–838 (2007). doi:10.1111/j.1365-246X.2007.03462.x

34. C. G. L. Bassin, G. Laske, G. Masters, paper presented at the 2000 American Geophysical Union Fall Meeting, San Francisco, CA, 15 December 2000.

35. A. Fichtner, H. Igel, Efficient numerical surface wave propagation through the optimization of discrete crustal models-a technique based on non-linear dispersion curve matching (DCM). *Geophys. J. Int.* **173**, 519–533 (2008). doi:10.1111/j.1365-246X.2008.03746.x

36. M. H. Ritzwoller, N. M. Shapiro, M. P. Barmin, A. L. Levshin, Global surface wave diffraction tomography. *J. Geophys. Res.* **107**, 2335 (2002). doi:10.1029/2002JB001777

37. N. Shapiro, M. Ritzwoller, Monte-Carlo inversion for a global shear-velocity model of the crust and upper mantle. *Geophys. J. Int.* **151**, 88–105 (2002). doi:10.1046/j.1365-246X.2002.01742.x

38. T. M. Brocher, Empirical Relations between Elastic Wavespeeds and Density in the Earth's Crust. *Bull. Seismol. Soc. Am.* **95**, 2081–2092 (2005). doi:10.1785/0120050077

39. A. Tarantola, B. Valette, Generalized nonlinear inverse problems solved using the least squares criterion. *Rev. Geophys.* **20**, 219–232 (1982). doi:10.1029/RG020i002p00219

40. X. D. Li, B. Romanowicz, Comparison of global waveform inversions with and without considering cross-branch modal coupling. *Geophys. J. Int.* **121**, 695–709 (1995). doi:10.1111/j.1365-246X.1995.tb06432.x

41. J. Tromp, C. Tape, Q. Liu, Seismic tomography, adjoint methods, time reversal and banana-doughnut kernels. *Geophys. J. Int.* **160**, 195–216 (2005). doi:10.1111/j.1365-246X.2004.02453.x

42. Z. Wang, F. A. Dahlen, Spherical-spline parameterization of three-dimensional earth models. *Geophys. Res. Lett.* **22**, 3099–3102 (1995). doi:10.1029/95GL03080

43. C. Mégnin, B. Romanowicz, The three-dimensional shear velocity structure of the mantle from the inversion of body, surface and higher-mode waveforms. *Geophys. J. Int.* **143**, 709–728 (2000). doi:10.1046/j.1365-246X.2000.00298.x

44. M. Panning, B. Romanowicz, A three-dimensional radially anisotropic model of shear velocity in the whole mantle. *Geophys. J. Int.* **167**, 361–379 (2006). doi:10.1111/j.1365-246X.2006.03100.x

45. G. Laske, G. Masters, Constraints on global phase velocity maps from long-period polarization data. *J. Geophys. Res.* **101**, 16059–16075 (1997). doi:10.1029/96JB00526

46. G. Ekström, A global model of Love and Rayleigh surface wave dispersion and anisotropy, 25-250 s. *Geophys. J. Int.* **187**, 1668–1686 (2011). doi:10.1111/j.1365-246X.2011.05225.x

47. B. Kustowski, G. Ekström, A. M. Dziewonski, Anisotropic shear-wave velocity structure of the Earth's mantle: A global model. *J. Geophys. Res.* **113**, B06306 (2008). doi:10.1029/2007JB005169

48. J. Ritsema, A. Deuss, H. J. van Heijst, J. H. Woodhouse, S40RTS: a degree-40 shear-velocity model for the mantle from new Rayleigh wave dispersion, teleseismic traveltime and normal-mode splitting function measurements. *Geophys. J. Int.* **184**, 1223–1236 (2011). doi:10.1111/j.1365-246X.2010.04884.x

49. N. Harmon, D. W. Forsyth, D. S. Weeraratne, Thickening of young Pacific lithosphere from high-resolution Rayleigh wave tomography: A test of the conductive cooling model. *Earth Planet. Sci. Lett.* **278**, 96–106 (2009). doi:10.1016/j.epsl.2008.11.025

50. J. MacQueen, in Proc. Fifth Berkeley Symp. on Math. Statist. and Prob **1**, 281–297 (1967).

51. A. Tarantola, *Inverse Problem Theory and Methods for Model Parameter Estimation*, (SIAM, Philadelphia, 2005).

52. J. Lévěque, L. Rivera, G. Wittlinger, On the use of the checker-board test to assess the resolution of tomographic inversions. *Geophys. J. Int.* **115**, 313–318 (1993). doi:10.1111/j.1365-246X.1993.tb05605.x

53. B. Efron, R. J. Tibishirani, *An Introduction to Bootstrap* (Chapman and Hall, New York, 1991).

54. X. D. Li, B. Romanowicz, Global mantle shear velocity model developed using nonlinear asymptotic coupling theory. *J. Geophys. Res.* **101**, 22,245–22,272 (1996). doi:10.1029/96JB01306

55. A. E. Gripp, R. G. Gordon, Young tracks of hotspots and current plate velocities. *Geophys. J. Int.* **150**, 321–361 (2002). doi:10.1046/j.1365-246X.2002.01627.x

56. L. Stixrude, C. Lithgow-Bertelloni, Mineralogy and elasticity of the oceanic upper mantle: Origin of the low-velocity zone. *J. Geophys. Res.* **110**, B03204 (2005). doi:10.1029/2004JB002965

57. F. Cammarano, B. Romanowicz, L. Stixrude, C. Lithgow-Bertelloni, W. Xu, Inferring the thermochemical structure of the upper mantle from seismic data. *Geophys. J. Int.* **179**, 1169–1185 (2009). doi:10.1111/j.1365-246X.2009.04338.x

58. M. M. Hirschmann, Mantle solidus: Experimental constraints and the effects of peridotite composition. *Geochem. Geophys. Geosyst.* **1**, GC000070 (2000). doi:10.1029/2000GC000070

59. D. M. Christie, B. P. West, D. G. Pyle, B. B. Hanan, *Nature* **394**, 637–644 (1998). doi:10.1038/29226

60. J. P. Montagner, N. Jobert, Investigation of upper mantle structure under young regions of the southeast Pacific using long-period Rayleigh waves. *Phys. Earth Planet. Inter.* **27**, 206–222 (1981). doi:10.1016/0031-9201(81)90017-0